LUMINOSITY FUNCTIONS OF LYMAN BREAK GALAXIES AT $z \sim 4$ AND $z \sim 5$ IN THE SUBARU DEEP FIELD[1]

Makiko Yoshida,[2] Kazuhiro Shimasaku,[2,3] Nobunari Kashikawa,[4,5] Masami Ouchi,[6,7] Sadanori Okamura,[2,3] Masaru Ajiki,[8] Masayuki Akiyama,[9] Hiroyasu Ando,[4] Kentaro Aoki,[9] Mamoru Doi,[10] Hisanori Furusawa,[9] Tomoki Hayashino,[11] Fumihide Iwamuro,[12] Masanori Iye,[4,5] Hiroshi Karoji,[12] Naoto Kobayashi,[10] Keiichi Kodaira,[13] Tadayuki Kodama,[4] Yutaka Komiyama,[4] Matthew A. Malkan,[14] Yuichi Matsuda,[12] Satoshi Miyazaki,[9] Yoshihiko Mizumoto,[4] Tomoki Morokuma,[10] Kentaro Motohara,[10] Takashi Murayama,[8] Tohru Nagao,[4,15] Kyoji Nariai,[16] Kouji Ohta,[12] Toshiyuki Sasaki,[9] Yasunori Sato,[4] Kazuhiro Sekiguchi,[9] Yasuhiro Shioya,[8] Hajime Tamura,[11] Yoshiaki Taniguchi,[8] Masayuki Umemura,[17] Toru Yamada,[4] and Naoki Yasuda[18]
Received 2005 December 17; accepted 2006 August 22

ABSTRACT

We investigate the luminosity functions of Lyman break galaxies (LBGs) at $z \sim 4$ and $z \sim 5$ based on optical imaging data obtained in the Subaru Deep Field project. Three samples of LBGs in a contiguous area of 875 arcmin^2 are constructed. One consists of 3808 LBGs at $z \sim 4$ down to $i' = 26.85$ selected with the $B-R$ versus $R-i'$ diagram. The other two consist of 539 and 240 LBGs at $z \sim 5$ down to $z' = 26.05$ selected with two kinds of two-color diagram: $V-i'$ versus $i'-z'$ and $R-i'$ versus $i'-z'$. The adopted selection criteria are proved to be fairly reliable by spectroscopic observations. We derive the luminosity functions of the LBGs at rest-frame ultraviolet wavelengths down to $M_{\rm UV} = -19.2$ at $z \sim 4$ and $M_{\rm UV} = -20.3$ at $z \sim 5$. We find clear evolution of the luminosity function over the redshift range $0 \leq z \leq 6$, which is accounted for solely by a change in the characteristic magnitude M^*. We examine the evolution of the cosmic star formation rate (SFR) density and its luminosity dependence over $0 \leq z \lesssim 6$. The SFR density contributed from brighter galaxies is found to change more drastically with cosmic time. The contribution from brighter galaxies has a sharp peak around $z = 3$–4, while that from fainter galaxies evolves relatively mildly with a broad peak at earlier epochs. Combining the observed SFR density with the standard cold dark matter model, we compute the cosmic SFR per unit baryon mass in dark halos, that is, the specific SFR. The specific SFR is found to scale with redshift as $(1 + z)^3$ up to $z \sim 4$, implying that the efficiency of star formation is on average higher at higher redshift in proportion to the cooling rate within dark halos, while this is not simply the case at $z \gtrsim 4$.

Subject headings: cosmology: observations — galaxies: evolution — galaxies: high-redshift — galaxies: luminosity function, mass function

1. INTRODUCTION

When and how galaxies formed is one of the primary questions in astronomy today. Observations of young galaxies at high redshifts are a straightforward approach to this problem. Over the past decade, it has become feasible to undertake large surveys of galaxies at high redshifts. This was made possible by progress in observing technology, including telescopes and detectors, and also in sophistication of selection methods to locate high-redshift galaxies. Probably the most efficient method is the Lyman break technique, a simple photometric approach based on the continuum features in rest-frame ultraviolet spectra redshifted into optical bandpasses, which requires only optical imaging in a few bands. Pioneered by Guhathakurta et al. (1990), this method has been successfully used to find many young, star-forming galaxies beyond $z \sim 2$ (e.g., Steidel & Hamilton 1992; Steidel et al. 1999; Lehnert & Bremer 2003; Iwata et al. 2003; Ouchi et al. 2004; Dickinson et al. 2004; Sawicki & Thompson 2006). Steidel et al.

[1] Based on data collected at the Subaru Telescope, which is operated by the National Astronomical Observatory of Japan.
[2] Department of Astronomy, Graduate School of Science, University of Tokyo, 7-3-1 Hongo, Bunkyo-ku, Tokyo 113-0033, Japan; myoshida@astron.s.u-tokyo.ac.jp.
[3] Research Center for the Early Universe, Graduate School of Science, University of Tokyo, 7-3-1 Hongo, Bunkyo-ku, Tokyo 113-0033, Japan.
[4] Optical and Infrared Astronomy Division, National Astronomical Observatory of Japan, 2-21-1 Osawa, Mitaka, Tokyo 181-8588, Japan.
[5] Department of Astronomical Science, School of Physical Sciences, Graduate University for Advanced Studies (Sokendai), 2-21-1 Osawa, Mitaka, Tokyo 181-8588, Japan.
[6] Space Telescope Science Institute, 3700 San Martin Drive, Baltimore, MD 21218.
[7] Hubble Fellow.
[8] Astronomical Institute, Graduate School of Science, Tohoku University, Aramaki, Aoba-ku, Sendai 980-8578, Japan.
[9] Subaru Telescope, National Astronomical Observatory of Japan, 650 North A'ohoku Place, Hilo, HI 96720.
[10] Institute of Astronomy, Graduate School of Science, University of Tokyo, 2-21-1 Osawa, Mitaka, Tokyo 181-8588, Japan.
[11] Research Center for Neutrino Science, Graduate School of Science, Tohoku University, Aramaki, Aoba-ku, Sendai 980-8578, Japan.
[12] Department of Astronomy, Graduate School of Science, Kyoto University, Kitashirakawa, Oiwake-cho, Sakyo-ku, Kyoto 606-8502, Japan.
[13] Graduate University for Advanced Studies (Sokendai), Shonan Village, Hayama, Kanagawa 240-0193, Japan.
[14] Department of Physics and Astronomy, Box 951547, UCLA, Los Angeles, CA 90095.
[15] Osservatorio Astrofisico di Arcetri, INAF, Largo Enrico Fermi 5, I-50125 Florence, Italy.
[16] Department of Physics, Meisei University, 2-1-1 Hodokubo, Hino, Tokyo 191-8506, Japan.
[17] Center for Computational Physics, University of Tsukuba, 1-1-1 Tennodai, Tsukuba, Ibaraki 305-8571, Japan.
[18] Institute for Cosmic Ray Research, University of Tokyo, Kashiwa, Chiba 277-8582, Japan.

(2003) made spectroscopic observations of about 1000 photometrically selected $z \sim 3$ galaxies and verified the usefulness of this method. High-redshift galaxies selected by this method are called Lyman break galaxies (LBGs).

Since their discovery in the 1990s, various properties of LBGs have been extensively studied. One of the most fundamental measurements is the luminosity function (LF) at rest-frame ultraviolet wavelengths (i.e., the number density of galaxies as a function of ultraviolet luminosity). Besides providing information on the number density of galaxies, the LF can be used to probe the star formation activity in the universe, because ultraviolet luminosity is sensitive to star formation. Thus, the ultraviolet luminosity density derived by integrating the LF is related to the star formation rate (SFR) density in the universe. By obtaining the LF at various redshifts and examining its evolution, one can gain insights into the formation history of galaxies and the star formation history in the universe.

Steidel et al. (1999) derived the LF at $z \sim 3$ from their large LBG sample, finding their data to be well fitted by a Schechter function with a low-luminosity slope α of -1.6 down to $L \simeq 0.1L^*$. They extended their LBG search to $z \sim 4$ and detected no significant evolution of the LF at bright magnitudes ($M < -21.1$) from $z \sim 4$ to $z \sim 3$. More recent observations have also derived the LF at $z \sim 4$ and $z \sim 5$ (Iwata et al. 2003; Ouchi et al. 2004; Gabasch et al. 2004; Sawicki & Thompson 2006). The frontier of LBG searches now extends beyond $z \sim 5$ (Yan et al. 2003; Stanway et al. 2003; Bunker et al. 2004; Bouwens et al. 2004, 2006; Shimasaku et al. 2005).

However, it is not easy to construct a large sample of LBGs beyond $z \sim 4$ covering a wide range in absolute magnitude, because of their apparent faintness and low surface number density. In the first place, most studies to date have been limited to bright LBGs. Consequently, the shape of the faint end of the LF has not been well determined. Thus, the estimate of the cosmic SFR density has a considerable uncertainty (about a factor of 3–10) due to the long extrapolation of the observed LFs to faint magnitudes (see Ouchi et al. 2004). Exploring LBGs down to faint luminosities is necessary in order to determine the overall shape of the LF and to measure the cosmic SFR density accurately. Although some surveys are extremely deep, they are restricted to very small areas (e.g., $\sim$4 arcmin^2 for the Hubble Deep Field, and $\sim$10 arcmin^2 for the Hubble Ultra Deep Field). Surveys based on such a small area probably suffer from cosmic variance, that is, inhomogeneities in the spatial distribution of LBGs. Although deep and wide surveys of LBGs at $z \sim 4$ have been made by Gabasch et al. (2004) and Sawicki & Thompson (2006) very recently, large samples for $z \gtrsim 4$ are still very limited. It is therefore crucial to construct a new LBG sample from a survey of a similar depth and width and derive the LF and the cosmic SFR independently.

In this paper, we present a detailed study of LBGs at $z \sim 4$–5 based on the deep, wide-field images obtained in the Subaru Deep Field (SDF) project (Kashikawa et al. 2004). The SDF project is a program conducted by Subaru Observatory to carry out a deep galaxy survey over a blank field as large as $\simeq$0.2 square degrees. Exploiting these unique data, we create the largest samples of LBGs at $z \sim 4$ and $z \sim 5$ and derive the LFs down to very faint magnitudes: $M_{\rm UV} = -19.2$ at $z \sim 4$ and $M_{\rm UV} = -20.3$ at $z \sim 5$. This extends the LBG search by Ouchi et al. (2004), based on shallower data from a smaller area of the same field, some $\sim$0.5 mag further and 1.5 times wider, leading to a factor of $\sim$3 increase in number of LBGs detected. These samples enable us to examine the behavior of the LF more accurately over a wide magnitude range and obtain more reliable measurements of the cosmic SFR density in the early universe. The LFs of LBGs at

$z \sim 4$ and $z \sim 5$ that we derive are found to differ from those at the same redshift ranges obtained in some of the previous surveys.

Recently, the LF at ultraviolet wavelengths of present-day galaxies ($z \sim 0$) has been derived very accurately from a large survey by the *Galaxy Evolution Explorer* (*GALEX*) (Wyder et al. 2005). Arnouts et al. (2005) have derived the LF at $0.2 \le z \le 1.2$, also based on *GALEX* observations. Measurements at $z \sim 6$ are now available (Shimasaku et al. 2005; Bouwens et al. 2006). Combining the results at $z \sim 4$ and $z \sim 5$ from this work with those at lower redshifts and at $z \sim 6$ from the literature, we investigate the evolutionary history of galaxies in terms of the star formation activity over $0 \le z \lesssim 6$.

The outline of this paper is as follows: Section 2 describes the data from the SDF project used in this study. Section 3 describes the selection of LBGs at $z \sim 4$ and $z \sim 5$ from the photometric data. The contamination by interlopers and the completeness of the samples are also estimated. In § 4, the rest-frame UV luminosity functions of LBGs at $z \sim 4$ and $z \sim 5$ are derived and compared with those of other authors. In § 5, we discuss the evolution of cosmic star formation activity over the redshift range $0 \le z \le 6$. The evolution of the LF and the cosmic SFR density is examined. Section 6 summarizes our work.

Throughout, the photometric system is based on AB magnitudes (Oke & Gunn 1983). The cosmology adopted is a flat universe with $\Omega_m = 0.3$, $\Omega_\Lambda = 0.7$, and a Hubble constant of $H_0 = 70$ km s^{-1} Mpc^{-1}. These values are consistent with those obtained from the latest observations of the cosmic microwave background (Spergel et al. 2003).

2. DATA

The data used in this study were obtained in the SDF project (Kashikawa et al. 2004). The program consists of very deep multiband optical imaging, near-infrared (NIR) imaging for smaller portions of the field, and follow-up optical spectroscopy. This study is based on the optical imaging data together with additional information from the spectroscopic data. Full details of the optical imaging observations, data reduction, and object detection and photometry are provided in Kashikawa et al. (2004).

2.1. *Imaging Data*

The optical imaging observations in the SDF project were carried out with the prime-focus camera (Suprime-Cam; Miyazaki et al. 2002) mounted on the 8.2 m Subaru Telescope (Iye et al. 2004) in 2002 and 2003. The imaging was made for a single Suprime-Cam field of view ($34' \times 27'$) toward the SDF (Maihara et al. 2001), centered on $13^{\rm h}24^{\rm m}38^{\rm s}9$, $+27°29'25''9$ (J2000). The scale of Suprime-Cam is $0''202$ pixel^{-1}. The images were taken in the five standard broadband filters B, V, R, i', and z' and two narrowband filters, NB816 and NB921. The central wavelengths of the broad bands are 4458, 5478, 6533, 7684, and 9037 Å, for B, V, R, i', and z', respectively. The SDF was previously imaged during the commissioning runs of Suprime-Cam in 2001 in B, V, R, i', and z', with 1–3 hr exposure times. The work by Ouchi et al. (2004) is based on those data. They were co-added in constructing the final images.

All individual CCD data with good quality were reduced and combined to make a single image for each band using a pipeline software package (Ouchi 2003) whose core programs were taken from IRAF and mosaic CCD data reduction software (Yagi et al. 2002). The combined images for all seven bands were aligned and smoothed with Gaussian kernels so that all have the same seeing size, a point-spread function (PSF) FWHM of $0''98$. The efficiency and reliability of object detection and photometry in
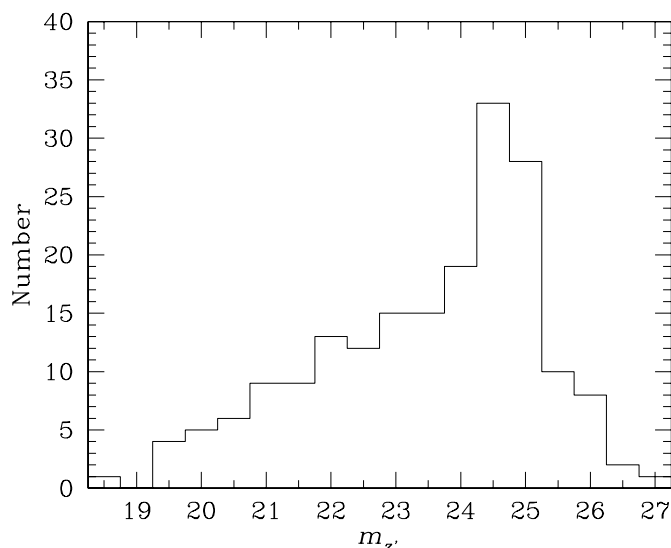
Fig. 1.—Magnitude distribution of the spectroscopic objects with $z_{spec} < 5.5$ in our catalogs.

Fig. 2.—Redshift distribution of the spectroscopic objects with $z_{spec} < 5.5$ in our catalogs.

regions near the edges of the images are significantly lower on account of low signal-to-noise ratios caused by dithering. Regions around very bright stars are also degraded because of bright halos and saturation trails. We carefully defined these low-quality regions and did not use objects located in them. The effective area of the final images after removal of the low-quality regions is 875 arcmin^2. Photometric calibration for the images was accomplished using measurements of standard stars taken during the observations. The total exposure time reaches ~10 hr for each band, and the limiting magnitudes (3 σ within a 2″ diameter aperture) are 28.45 (B), 27.74 (V), 27.80 (R), 27.43 (i'), 26.62 (z'), 26.63 (NB816), and 26.54 (NB921).

Object detection and photometry were performed using SExtractor version 2.1.6 (Bertin & Arnouts 1996). A collection of at least five contiguous pixels above the 2 σ sky noise was identified as an object. The object detection was carried out for all seven images independently. For each of the objects detected in a given band, photometry was performed on all the images at exactly the same position as in the detection-band image. Thus, seven catalogs were constructed for the respective detection bands. For the present study, we limit the catalogs to objects whose detection-band magnitudes are brighter than the 5 σ limiting magnitude (5 σ sky noise within a 2″ diameter aperture) of that band, in order to provide a reasonable level of photometric completeness. We use magnitudes within a 2″ diameter aperture to derive the colors of objects and adopt MAG_AUTO in SExtractor for total magnitudes. The magnitudes of objects were corrected for a small amount of foreground Galactic extinction toward the SDF using the dust map of Schlegel et al. (1998). Since the variation of $E(B-V)$ over the 875 arcmin^2 of the SDF is at most 0.007, we adopt a single value, $E(B-V) = 0.017$, for correction, which is the value at the center of the field. This corresponds to extinctions of $A_B = 0.07$, $A_V = 0.05$, $A_R = 0.04$, $A_{i'} = 0.03$, $A_{z'} = 0.02$, $A_{NB816} = 0.03$, and $A_{NB921} = 0.02$.

2.2. Spectroscopic Data

We carried out spectroscopic follow-up observations for some objects in our catalogs with the Faint Object Camera and Spectrograph (FOCAS; Kashikawa et al. 2002) on the Subaru Telescope during 2002–2004 and with DEIMOS (Faber et al. 2003) on the Keck II Telescope in 2004. The spectroscopic observations were made in the multiobject slit mode. For the FOCAS ob-
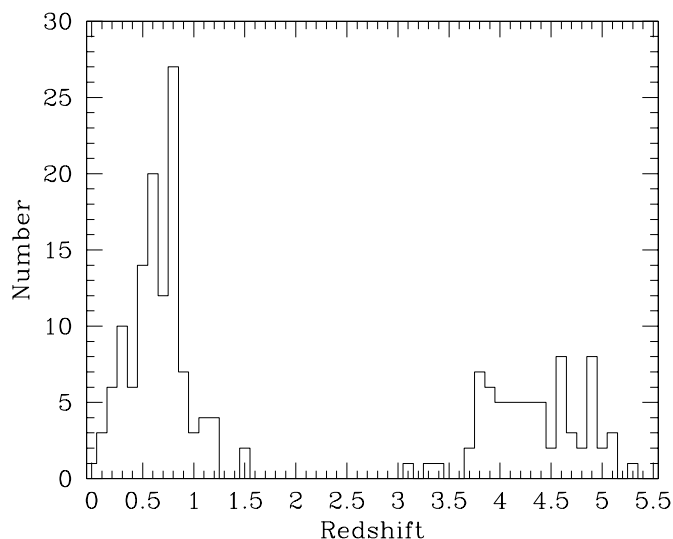
servations, we used a 300 line mm^{-1} grating with an O58 order-cut filter and an echelle with a z' filter. Slit widths on the masks were either 0″8 or 0″6 for the 300-line configuration, resulting in a spectral resolution of 9.5 or 7.1 Å at 8150 Å, respectively, and 0″8 for the echelle. The integration times for the respective masks were 7000–9000 s. Flux calibration was carried out with spectra of the spectroscopic standard stars HZ 44 and Feige 34. The data were reduced in a standard manner. For the observations with DEIMOS, we used an 830 line mm^{-1} grating with a GG 495 order-cut filter. Slit widths were 1″0, which gave a spectral resolution of 3.97 Å. The integration times were 6300–19,800 s. Spectra of the standard stars BD +28 4211 and Feige 110 were taken for flux calibration. The data were reduced with the spec2d pipeline,[19] developed for the reduction of DEIMOS data in the DEEP2 survey. In addition, we also use spectra of objects in the SDF that were taken during FOCAS guaranteed time observations in 2001 (Kashikawa et al. 2003; Ouchi et al. 2004).

In Figures 1 and 2, we present the distributions of the z' magnitudes of the spectroscopic objects and their redshifts, respectively. Only objects with $z_{spec} < 5.5$ are included here.

3. LYMAN BREAK GALAXY SAMPLES AT $z \sim 4$ AND $z \sim 5$

3.1. Selection of Lyman Break Galaxies

We demonstrate the principle of the Lyman break color selection technique to locate galaxies at $z \sim 4$ and $z \sim 5$ in Figure 3. For galaxies at $z \sim 4$, the break in the spectrum at rest-frame UV wavelength enters the B band, and the flat continuum longward of Lyα shifts to wavelengths longer than the R band; these galaxies are identifiable by their red $B-R$ color and blue $R-i'$ color. We select LBGs at $z \sim 4$ using these two colors (hereafter BRi' LBGs). For galaxies at $z \sim 5$, the spectral break enters into the V band and the flat continuum is sampled at wavelengths longer than the i' band. At $z \sim 5$, the attenuation due to the Lyα forest is so strong that the flux in the R band is severely suppressed, as is the flux in the V band. Thus, galaxies at $z \sim 5$ are identified by their red $V-i'$ or $R-i'$ color and blue $i'-z'$ color. We created two samples for LBGs at $z \sim 5$: one selected by $V-i'$
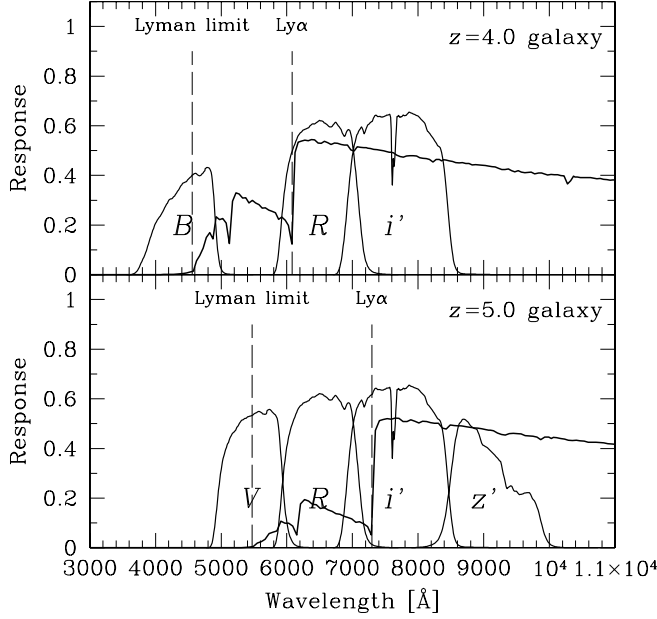

Fig. 3.—*Top*: The B, R, and i' bandpasses overplotted on the spectrum of a generic $z = 4$ galaxy (*thick line*), illustrating the utility of the color selection technique with these three bandpasses for locating $z \sim 4$ galaxies. *Bottom*: The V, R, i', and z' bandpasses overplotted on the spectrum of a generic $z = 5$ galaxy (*thick line*). The sets $Vi'z'$ and $Ri'z'$ work well to isolate $z \sim 5$ galaxies.

and $i'-z'$ colors, and the other selected by $R-i'$ and $i'-z'$ colors (hereafter $Vi'z'$ and $Ri'z'$ LBGs, respectively).

Figures 4–6 illustrate the predicted positions of high-redshift galaxies and foreground objects (lower redshift galaxies and Galactic stars) in three two-color diagrams: $B-R$ versus $R-i'$, $V-i'$ versus $i'-z'$, and $R-i'$ versus $i'-z'$. The solid lines in these figures indicate tracks for model spectra of young star-forming galaxies for the redshift range $z > 3$. The model spectra were constructed using the stellar population synthesis code developed by Kodama & Arimoto (1997). As model parameters an age of 0.1 Gyr, a Salpeter initial mass function, and a star formation timescale of 5 Gyr were adopted, and reddening of $E(B-V) = 0.16$ was applied using the dust extinction formula for starburst galaxies by Calzetti et al. (2000). These values reproduce the average rest-frame UV-optical spectral energy distribution of LBGs observed at $z \sim 3$ (Papovich et al. 2001). We also show tracks for model spectra with reddening $E(B-V)$ of 0 and 0.3 for reference. The absorption due to the intergalactic medium was applied following the prescription of Madau (1995). The dotted, dashed, and dot-dashed lines delineate the tracks for model spectra of local elliptical, spiral, and irregular galaxies, respectively, redshifted from $z = 0$ to $z = 3$. These spectra were also constructed using the Kodama-Arimoto population synthesis code and redshifted without evolution. The asterisks denote the 175 Galactic stars of various types whose spectra are given by Gunn & Stryker (1983). The colors were calculated by convolving constructed model spectra of galaxies or given spectra of stars with the response functions of the Suprime-Cam filters. It can be seen that the model young star-forming galaxy moves nearly vertically from the origin in these two-color diagrams at $z > 3$—namely, it becomes redder in $B-R$, $V-i'$, and $R-i'$, while keeping blue $R-i'$, $i'-z'$, and $i'-z'$ colors, as redshift increases—and that it shifts into a portion of the two-color space that is unpopulated by foreground objects. At $z > 5$ the $R-i'$ color does not become much redder, while $i'-z'$ becomes redder in the $R-i'$ versus $i'-z'$ diagram. These figures imply that LBGs at $z \sim 4$, and those at $z \sim 5$, can be well isolated from foreground objects in the $B-R$ versus $R-i'$ diagram, and in the
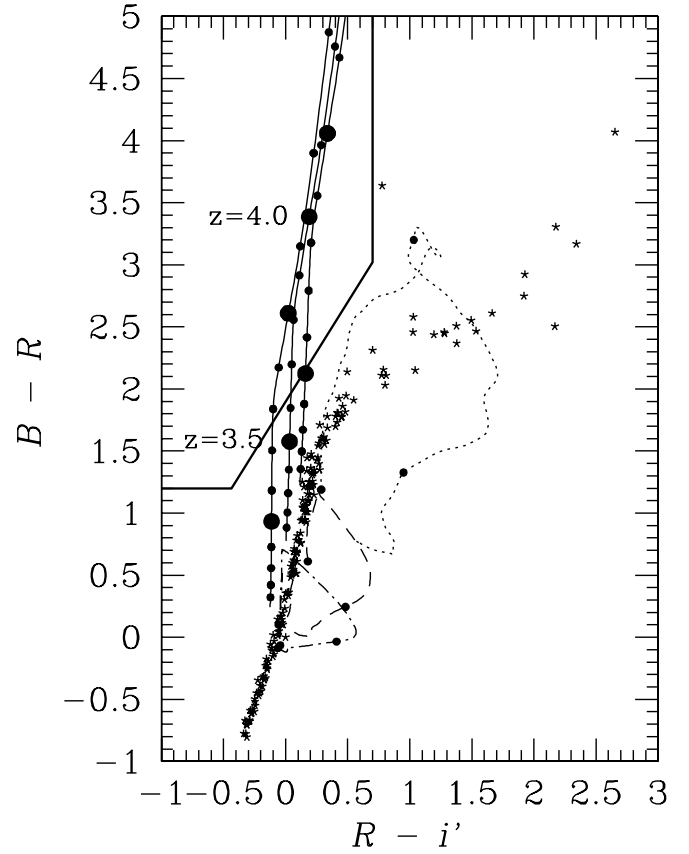

Fig. 4.—A $B-R$ vs. $R-i'$ diagram illustrating the predicted colors of model galaxies and stars. The three solid lines indicate the tracks for model spectra of young star-forming galaxies with reddening of $E(B-V) = 0$, 0.16, and 0.3 (*left to right*). The redshift range is from $z = 3$ to higher redshifts, and the circles on the track mark redshift intervals of 0.1. The dotted, dashed, and dot-dashed lines delineate the tracks for model spectra of local elliptical, spiral, and irregular galaxies, respectively, redshifted from $z = 0$ to $z = 3$ without evolution. The circles on each track mark $z = 0$, 1, and 2. The asterisks represent the colors of 175 Galactic stars given by Gunn & Stryker (1983). The thick line indicates the boundary that we adopt for the selection of BRi' LBGs.

$V-i'$ versus $i'-z'$ and $R-i'$ versus $i'-z'$ diagrams, respectively. The most critical contamination is caused by elliptical galaxies at $z \sim 0.5$, which come close to high-redshift galaxies in these diagrams as a result of the 4000 Å break in their spectra.

In Figures 7–9, we show the distribution of all the objects contained in the catalogs in the two-color diagrams. When the magnitude of an object in a nondetection band is fainter than the 1 σ magnitude of the band, the 1 σ magnitude is assigned to the object. Objects with spectroscopic redshifts are shown with colored symbols in these figures, where different colors indicate different redshift bins. The colors of the spectroscopically identified objects match up fairly well with those of the model galaxies at the corresponding redshifts in Figures 4–6.

We adopt the same color criteria for BRi' and $Vi'z'$ LBGs as used in Ouchi et al. (2004). For $Ri'z'$ LBGs, we visually fine-tuned the color criteria based on the increased redshift information. Specifically, we set the selection criteria for BRi' LBGs as

$$B-R > 1.2, \quad R-i' < 0.7, \quad B-R > 1.6(R-i') + 1.9, \quad (1)$$

for $Vi'z'$ LBGs as

$$V-i' > 1.2, \quad i'-z' < 0.7, \quad V-i' > 1.8(i'-z') + 1.7, \quad (2a)$$
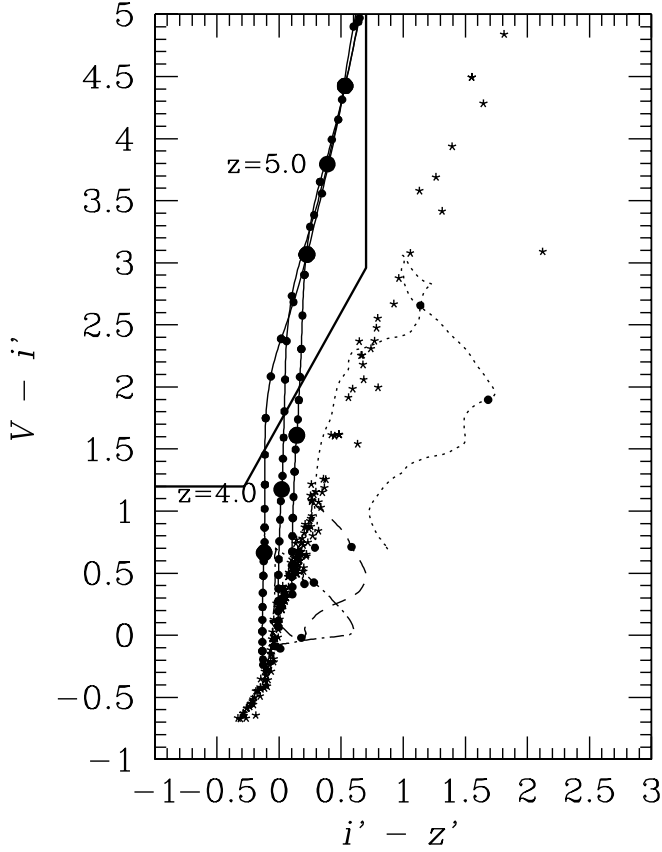$$B > 3 \; \sigma \; \text{mag}, \quad (2b)$$

Fig. 5.—A $V-i'$ vs. $i'-z'$ diagram illustrating the predicted colors of model galaxies and stars. Lines and symbols are the same as in Fig. 4. The thick line indicates the boundary that we adopt for the selection of $Vi'z'$ LBGs.
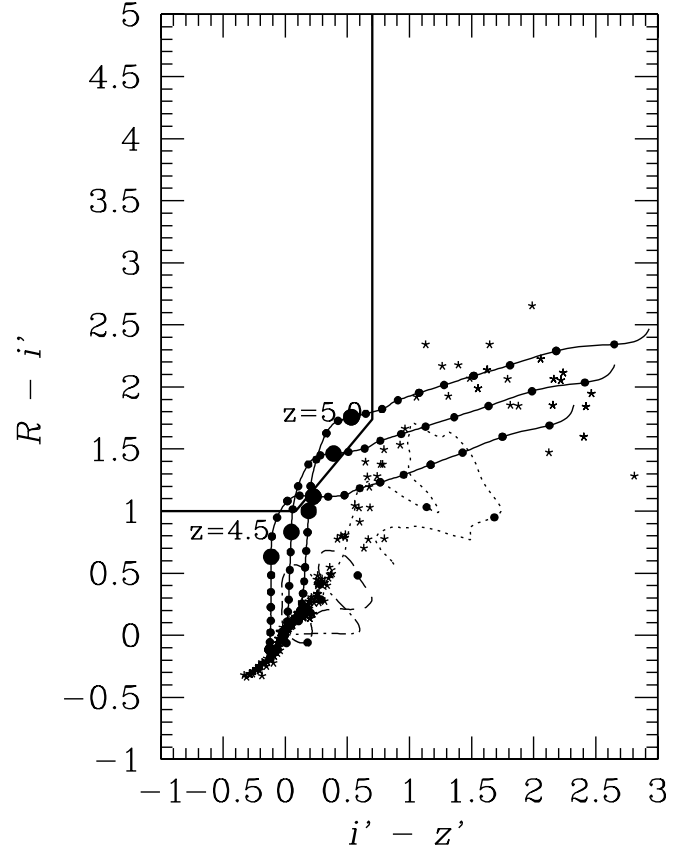

Fig. 6.—A $R-i'$ vs. $i'-z'$ diagram illustrating the predicted colors of model galaxies and stars. Lines and symbols are the same as in Fig. 4. The thick line indicates the boundary that we adopt for the selection of $Ri'z'$ LBGs.
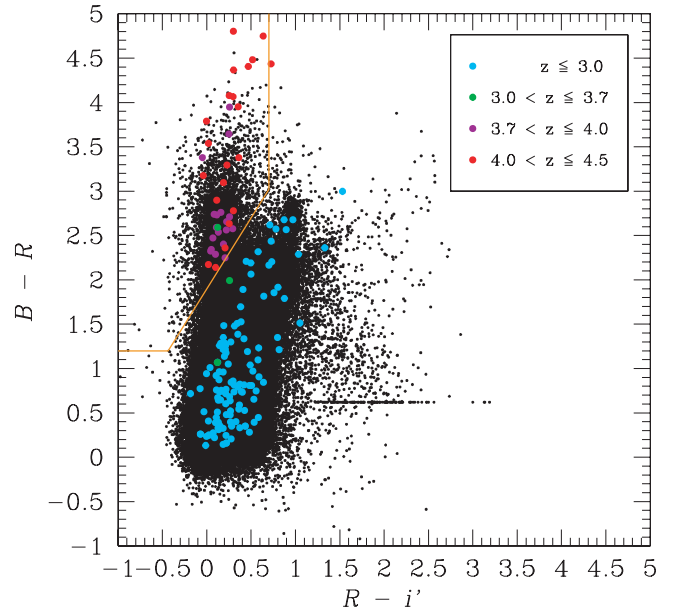
and for $Ri'z'$ LBGs as

$$R-i' > 1.0, \quad i'-z' < 0.7, \quad R-i' > 1.2(i'-z') + 0.9, \quad \text{(3a)}$$

$$(B, V) > 3 \, \sigma \, \text{mag}. \quad \text{(3b)}$$

The boundaries in the two-color diagrams defined by these color criteria are outlined in Figures 4–6 and Figures 7–9 (*orange*). For the bands placed entirely shortward of the Lyman break, we additionally require that LBGs should be undetected (criteria [2b] and [3b]), which is expected to work effectively to reduce contamination from foreground galaxies.

We applied these selection criteria to the catalogs. We use the i'-detection catalogs for BRi' LBGs, which contain 106,025 objects to a limit of $i' = 26.85$ (total magnitude corrected for Galactic extinction), and the z'-detection catalogs for $Vi'z'$ and $Ri'z'$ LBGs, which contain 76,351 objects to $z' = 26.05$ (total magnitude corrected for Galactic extinction). The number of objects that satisfy the selection criteria—that is, the number of LBG candidates—is 3808 for BRi' LBGs, 539 for $Vi'z'$ LBGs, and 240 for $Ri'z'$ LBGs.[20] Table 1 summarizes the samples of LBG candidates.

The selection criteria are shown by our spectroscopy to be fairly reliable. We spectroscopically observed 105 objects in the

Fig. 7.—A $B-R$ vs. $R-i'$ diagram for all the objects contained in the i'-detection catalogs (106,025 objects down to $i' \leq 26.85$). When the B or R magnitude of an object is fainter than the 1 σ magnitude of the band, the 1 σ magnitude is assigned to the object. The horizontal sequence along $B-R = 0.62$ shows objects that are fainter than the 1 σ magnitude in both B and R. The colored symbols show objects with spectroscopic redshifts, where cyan, green, violet, and red represent objects in the ranges $z < 3.0$, $3.0 \leq z < 3.7$, $3.7 \leq z < 4.0$, and $4.0 \leq z < 4.5$, respectively. The thick orange line indicates the boundary that we adopt for the selection of BRi' LBGs.

---

[20] For this study, we limit the catalogs to the 5 σ limiting magnitude. Kashikawa et al. (2006) also use our LBG samples for their study on the clustering properties of LBGs, but down to the 3 σ limiting magnitude. The number of LBG candidates with magnitudes brighter than the 3 σ limiting magnitude is 4543 for BRi' LBGs, 831 for $Vi'z'$ LBGs, and 386 for $Ri'z'$ LBGs. This difference causes no significant effect on the luminosity functions except for the faintest bins.
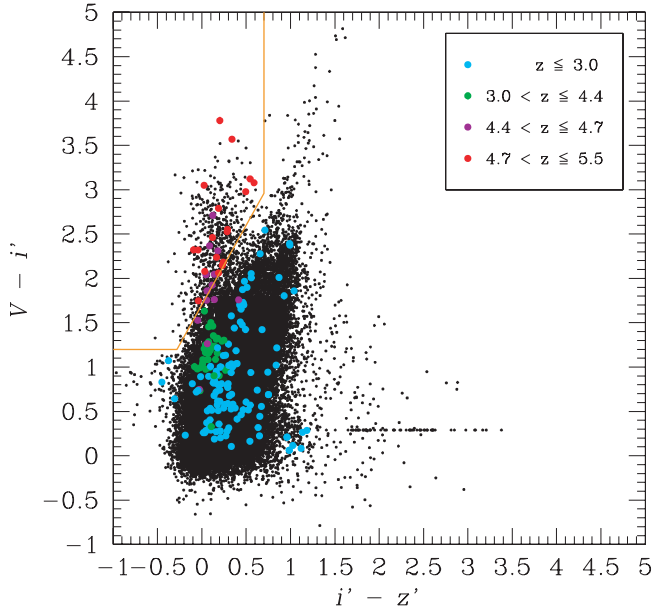
FIG. 8.—A $V-i'$ vs. $i'-z'$ diagram for all the objects contained in the z'-detection catalogs (76,351 objects down to $z' \leq 26.05$). When the V or i' magnitude of an object is fainter than the 1 σ magnitude of the band, the 1 σ magnitude is assigned to the object. The horizontal sequence along $V-i' = 0.29$ shows objects that are fainter than the 1 σ magnitude in both V and i'. The colored symbols show objects with spectroscopic redshifts, where cyan, green, violet, and red represent objects in the ranges $z < 3.0$, $3.0 \leq z < 4.4$, $4.4 \leq z < 4.7$, and $4.7 \leq z < 5.5$, respectively. The thick orange line indicates the boundary that we adopt for the selection of $Vi'z'$ LBGs.
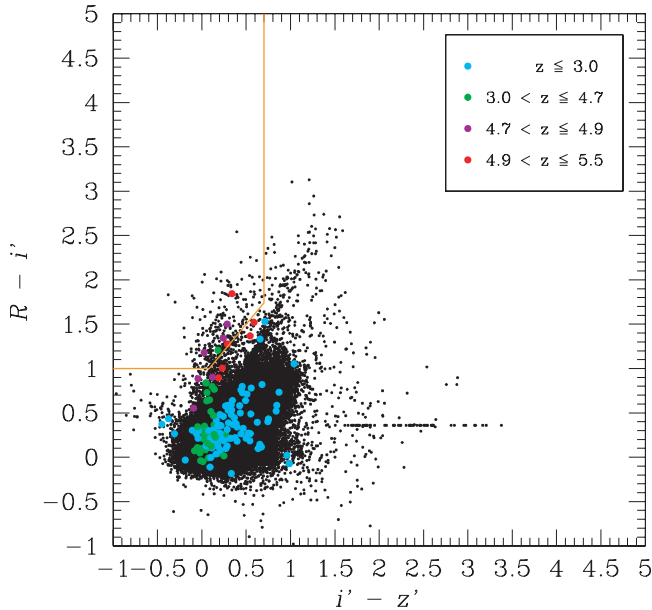

FIG. 9.—A $R-i'$ vs. $i'-z'$ diagram for all the objects contained in the z'-detection catalogs (76,351 objects down to $z' \leq 26.05$). When the R or i' magnitude of an object is fainter than the 1 σ magnitude of the band, the 1 σ magnitude is assigned to the object. The horizontal sequence along $R-i' = 0.35$ shows objects that are fainter than the 1 σ magnitude in both R and i'. The colored symbols show objects with spectroscopic redshifts, where cyan, green, violet, and red represent objects in the ranges $z < 3.0$, $3.0 \leq z < 4.7$, $4.7 \leq z < 4.9$, and $4.9 \leq z < 5.5$, respectively. The thick orange line indicates the boundary that we adopt for the selection of $Ri'z'$ LBGs.

TABLE 1
SAMPLES OF LBG CANDIDATES

Sample	Candidates	Detection Band	Magnitude Range[a]
BRi' LBGs................	3808	i'	$i' = 22.85–26.85$
$Vi'z'$ LBGs................	539	z'	$z' = 23.55–26.05$
$Ri'z'$ LBGs................	240	z'	$z' = 24.05–26.05$

[a] Total magnitudes corrected for Galactic extinction.

BRi' LBG sample and identified 42 objects. Among the 42 only one is an interloper, at $z = 3.29$, with the remaining 41 being at $z \geq 3.7$. Similarly, 32 objects from the $Vi'z'$ LBG sample were spectroscopically observed, and 23 were identified. All but one of the 23 objects are at $z \geq 4.4$; the remaining object appears to be a Galactic star. In the $Ri'z'$ LBG sample, 12 objects were spectroscopically observed and nine were identified. All are found to be at $z \geq 4.5$. Possible reasons for the low detection rate for BRi' LBGs are that the Lyα emission of $z \sim 4$ LBGs is on average weaker than that of $z \sim 5$ LBGs and that the Lyα line at $z \sim 4$ falls in a wavelength range where the sensitivity of our spectroscopy is relatively low. The failed sample may also include interlopers between $z \sim 2$ and $z \sim 3$ whose strong line features do not enter the wavelength coverage of our spectrograph. From the following simulation, however, we infer that the fraction of such interlopers is not so high in our LBG sample: First, we added noise to the colors of all objects outside of the BRi' selection criteria in our photometric catalog according to their measured magnitudes. We then counted the objects that met the selection criteria as a result of the modified colors and found that they were fewer than 10% of the original LBG candidates, even for the faintest magnitude bin, where photometric errors are the largest. Note that this simulation gives an upper limit to the fraction of interlopers, since the measured colors already include photometric errors. In Figure 10, we present the apparent magnitude distribution of the spectroscopically identified objects in each LBG sample. Although the spectroscopic targeting is biased toward bright objects, we emphasize here that the spectroscopic samples also include faint objects and that there are no interlopers even among them. We cannot, however, rule out the possibility that there may be interlopers for which no redshift has been secured. Figure 11 shows the redshift distribution of the spectroscopic samples. The average redshift is $\langle z \rangle_{\rm spec} = 4.1$ for BRi' LBGs, $\langle z \rangle_{\rm spec} = 4.8$ for $Vi'z'$ LBGs, and $\langle z \rangle_{\rm spec} = 4.9$ for $Ri'z'$ LBGs. Example spectra of $z \sim 4$ LBGs and $z \sim 5$ LBGs are shown in Figures 12 and 13, respectively.

3.2. Number Counts

The observed number counts of the LBG candidates as a function of apparent magnitude are shown in Figures 14–16, along with those measured by other authors who selected similar LBGs. None of the data are corrected for contamination or incompleteness. Previous LBG surveys included in the figures are summarized in Table 2. Ouchi et al. (2004) used the same photometric system as used here to create samples of LBGs at $z \sim 4$ over a 543 arcmin^2 area and of LBGs at $z \sim 5$ over a 616 arcmin^2 area of the SDF. Steidel et al. (1999) carried out a search for LBGs at $z \sim 4$ using $G-\mathcal{R}$ and $\mathcal{R}-I$ colors in a total area of 828 arcmin^2 over 10 separate fields. Sawicki & Thompson (2006) have undertaken a survey of LBGs at $z \sim 4$ with the same photometric system and selection criteria that Steidel et al. (1999) used, but to a deeper magnitude, in the Keck Deep Fields, which cover a total area of 169 arcmin^2 and consist of five fields. Iwata
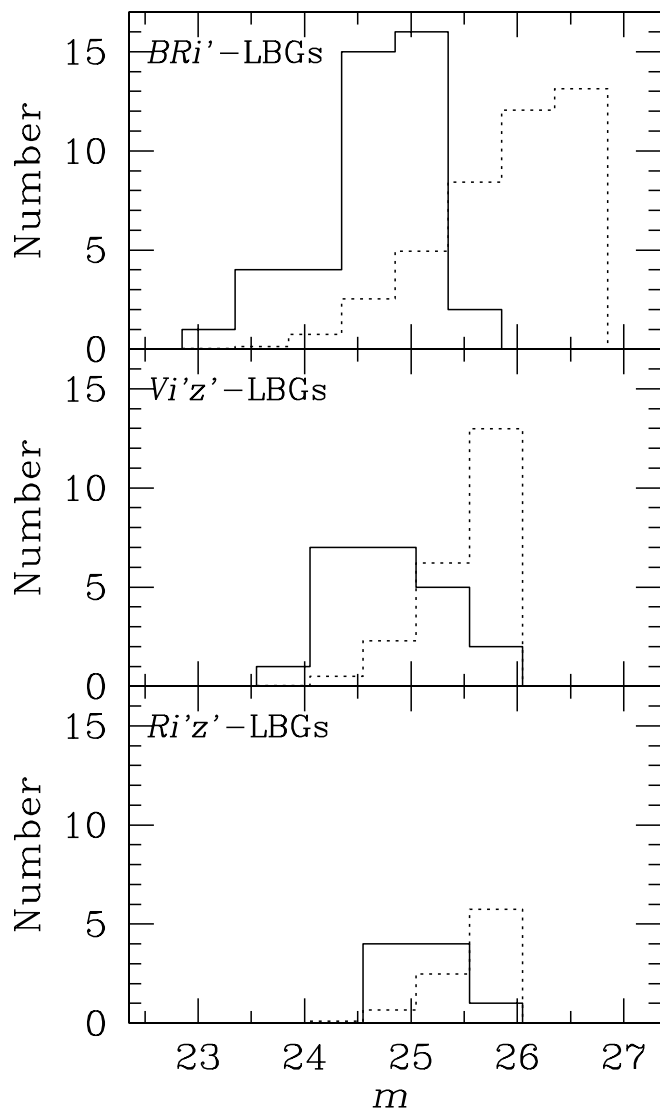
Fig. 10.— Magnitude distribution of the spectroscopically identified objects in each LBG sample (*solid histograms*). Dotted histograms show the magnitude distribution of all the objects in each LBG sample normalized to the number of spectroscopically identified objects.
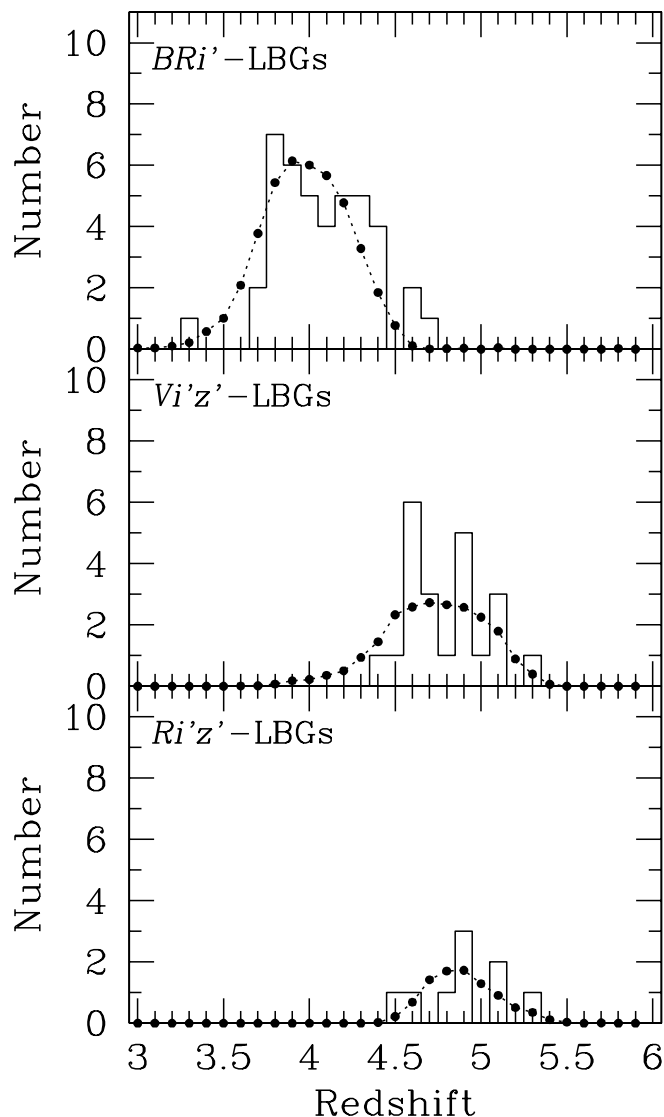

Fig. 11.— Redshift distribution of the spectroscopically identified objects in each LBG sample. Dotted lines show the redshift distribution functions from the Monte Carlo simulation (see § 3.3) normalized to the number of spectroscopically identified objects.

et al. (2003) found LBGs at $z \sim 5$ using $V - I_C$ and $I_C - z'$ colors in a 575 arcmin^2 area including the Hubble Deep Field North. Capak et al. (2004) obtained number counts of LBGs at $z \sim 4$ selected by $B - R$ and $R - I_C$ colors and LBGs at $z \sim 5$ selected by $V - I_C$ and $I_C - z'$ colors from a 720 arcmin^2 area centered on the Hubble Deep Field North. Our limiting magnitudes are among the faintest in LBG samples for $z \sim 4$ and $z \sim 5$ constructed to date.

In general, number-counts measurements of LBGs are dependent on detection completeness, photometric systems used, and selection criteria. We find that our counts match very well with those of Ouchi et al. (2004) for all the samples, aside from the brightest bins. While we use MAG_AUTO in SExtractor as the total magnitude of an object, Ouchi et al. (2004) calculated total magnitudes from aperture magnitudes through a fixed aperture correction of -0.2 mag. The correction value, however, actually can range to as much as -0.4 mag for bright LBGs. A shift of the Ouchi et al. magnitudes by -0.2 mag $[=-0.4 - (-0.2)]$ can settle the disagreement between those and our counts. The counts of Capak et al. (2004) are broadly lower than ours for $z \sim 4$ at faint magnitudes and for $z \sim 5$ at their faintest magnitude. The lower detection completeness of their data might be a

major cause of this inconsistency; the 5σ limiting magnitude of their data is about 1 mag brighter than that of the SDF project data. For $z \sim 4$ LBGs, our measurements agree with those of Steidel et al. (1999), although their measurements are limited to objects brighter than 25 mag. At faint magnitudes, however, our measurements are higher than those of Sawicki & Thompson (2006). For $z \sim 5$ LBGs, over a wide range of bright magnitudes ($m < 25$), a discrepancy is found between the counts of Iwata et al. (2003) and either ours or those of Capak et al. (2004), who surveyed almost the same field as Iwata et al.; the latter's counts are higher by a factor of $3-10$. The selection criteria of Iwata et al. are somewhat looser than ours. Therefore, as Ouchi et al. (2004) and Capak et al. (2004) claim, the LBG sample of Iwata et al. (2003) could be strongly contaminated by foreground galaxies.

3.3. Completeness

The completeness at a given apparent magnitude and redshift is defined as the ratio of LBGs that are detected and also pass the selection criteria to all the LBGs with the given apparent magnitude and redshift actually present in the universe. In general,
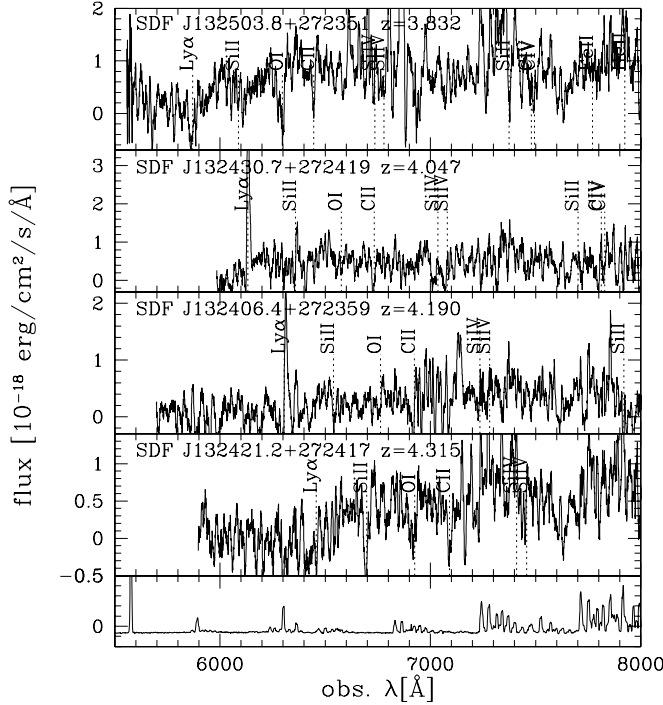
FIG. 12.—Examples of spectra of LBGs at $z \sim 4$ with good quality that have prominent spectral features such as a strong Lyα emission line and interstellar lines. The bottom panel shows a relative night-sky spectrum.

completeness decreases as apparent magnitude gets fainter and as redshift moves away from the central redshift of the sample. The completeness of each LBG sample is estimated as a function of apparent magnitude and redshift through a Monte Carlo simulation.

In the simulations, we generate artificial LBGs over an apparent magnitude range of $23.1 \leq m_{i'} \leq 26.6$ for BRi' LBGs and $23.8 \leq m_{z'} \leq 25.8$ for $Vi'z'$ and $Ri'z'$ LBGs with an interval of $\Delta m = 0.5$, and over a redshift range of $3.0 \leq z \leq 5.9$ with an interval of
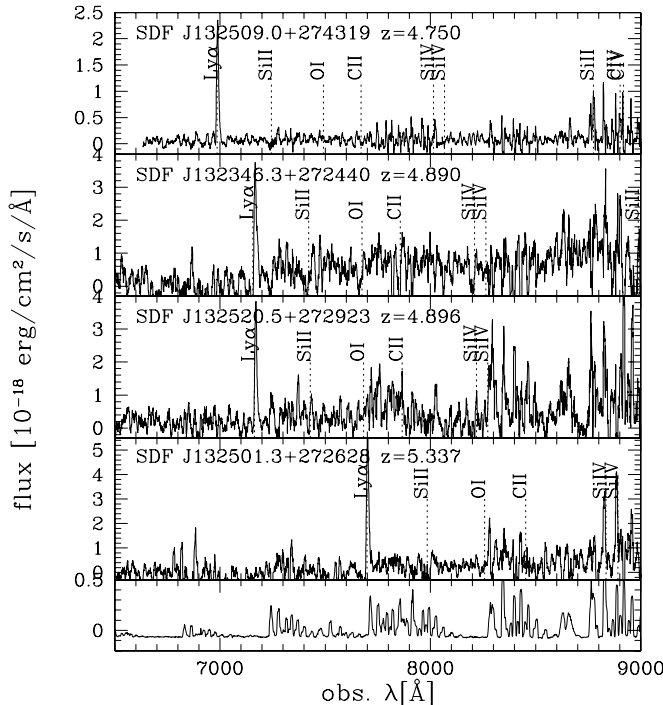

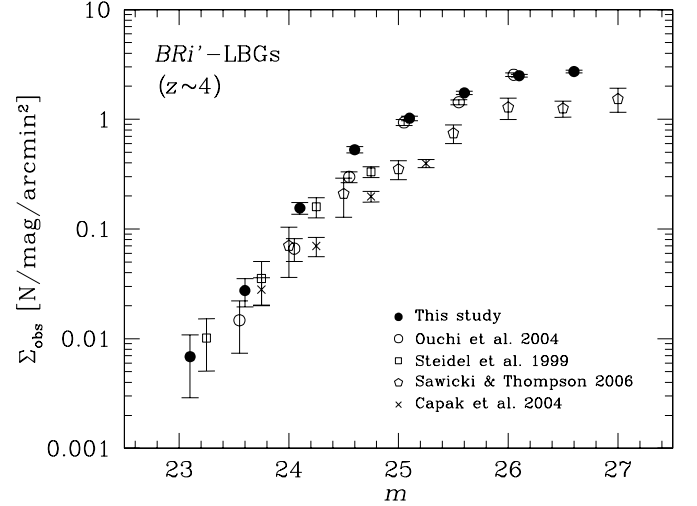FIG. 13.—Same as Fig. 12, but for $z \sim 5$.

FIG. 14.—Observed number counts of LBGs at $z \sim 4$, uncorrected for incompleteness or contamination. The filled circles represent the BRi' LBGs in this study. For comparison, we show the previous measurements obtained by Ouchi et al. (2004, *open circles*), Steidel et al. (1999, *squares*), Sawicki & Thompson (2006, *pentagons*), and Capak et al. (2004, *crosses*). The error bars for this study, Ouchi et al. (2004), and Capak et al. (2004) reflect Poisson errors. The error bars for Steidel et al. (1999) and Sawicki & Thompson (2006) include an estimate of cosmic variance from their multiple fields as well as Poisson errors.

$\Delta z = 0.1$. All LBGs are assumed to have the same intrinsic spectrum described in § 3.1, but with $E(B-V)$ values of 0.0, 0.1, 0.2, 0.3, and 0.4. Thus, 1200 ($8 \times 30 \times 5$) BRi' LBGs and 750 ($5 \times 30 \times 5$) $Vi'z'$ and $Ri'z'$ LBGs are generated. We assume that the shape of LBGs is PSF-like and assign apparent sizes to the artificial LBGs so that their size distribution measured by SExtractor (the peak FWHM is $\approx 1''00-1''04$) matches that of the observed LBG candidates. The artificial LBGs are then distributed randomly on the original images after adding Poisson noise according to their magnitudes, and object detection and photometry are performed in the same manner as was done for real objects. This process is repeated 100 times to obtain statistically accurate values of completeness. In each simulation, the completeness for a given apparent magnitude, redshift, and $E(B-V)$ value can be

FIG. 15.—Observed number counts of V-dropout LBGs at $z \sim 5$, uncorrected for incompleteness or contamination. The filled circles represent the $Vi'z'$ LBGs in this study. For comparison, we show the previous measurements obtained by Ouchi et al. (2004, *open circles*), Iwata et al. (2003, *triangles*), and Capak et al. (2004, *crosses*). The error bars reflect Poisson errors.
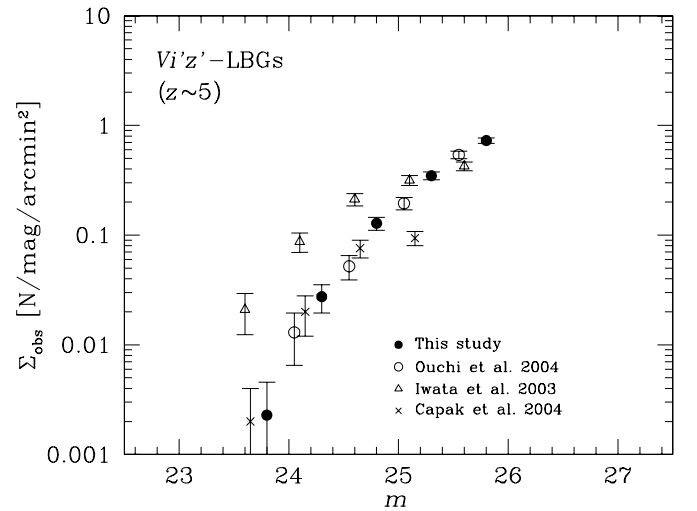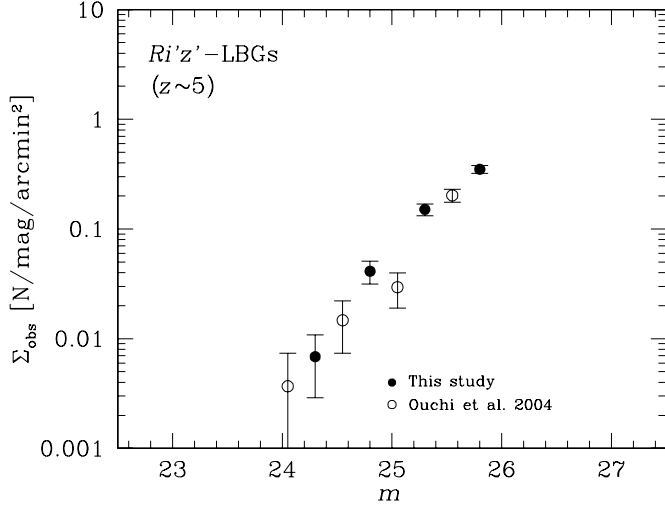
Fig. 16.—Observed number counts of R-dropout LBGs at $z \sim 5$ uncorrected for incompleteness or contamination. The filled circles represent the $Ri'z'$ LBGs in this study. For comparison, we show the previous measurements obtained by Ouchi et al. (2004, *open circles*). The error bars reflect Poisson errors.

defined as the ratio of the number of simulated LBGs that are detected and also satisfy the selection criteria to all the simulated objects with the given magnitude, redshift, and $E(B-V)$. We calculate the completeness of the LBG samples by taking a weighted average of the completeness for each of the five $E(B-V)$ values. The weight is taken using the $E(B-V)$ distribution function of $z \sim 4$ LBGs derived by Ouchi et al. (2004; see the solid histogram in their Fig. 20, *bottom*), which is corrected for incompleteness due to selection biases. We plot the recovered artificial objects in the two-color diagrams by taking the number of objects with each $E(B-V)$ value according to the adopted $E(B-V)$ distribution function. We verified that the distributions well resemble that of real objects. Hence, our modeling is reasonably realistic. The resulting completeness, $p(m, z)$, is shown in Figure 17.

In order to examine the uniformity of completeness over our images, we split the images into two regions (a center and a peripheral region), each with the same area, and recalculated the completeness for each region. The nonuniformity is found to be small; the variation between the center region and the periphery is within 10%.

For each of the three LBG samples, magnitude-weighted redshift distribution functions are derived from $p(m, z)$ (Fig. 17, *black lines*) by averaging the magnitude-dependent completeness weighted by the number of LBGs in each magnitude bin. The average redshift, $\bar{z}$, and its standard deviation, s_z, are calculated to be $\bar{z} = 4.0$ and $s_z = 0.3$ for BRi' LBGs, $\bar{z} = 4.7$ and $s_z = 0.3$ for $Vi'z'$ LBGs, and $\bar{z} = 4.9$ and $s_z = 0.2$ for $Ri'z'$ LBGs. We also compute magnitude-weighted redshift distribution functions, where the weighting is done by the number of spectroscopically identified LBGs (Fig. 11, *dotted lines*), to obtain average redshifts of $\bar{z}_{spec} = 4.0$ for BRi' LBGs, $\bar{z}_{spec} = 4.8$ for $Vi'z'$ LBGs, and $\bar{z}_{spec} = 4.9$ for $Ri'z'$ LBGs. These distribution functions are consistent with the redshift distributions of the spectroscopic samples shown in Figure 11.

Although the above modeling reproduces well the observed distribution of objects in the two-color diagrams and the observed redshift distribution functions, we further explored to what extent the results would be affected by adopting different models. To begin with, we recalculated the completeness using model spectra with two other ages, 0.01 and 0.5 Gyr, to find that the completeness changes by only a few percent. Then we examined two extreme cases of dust extinction, in which all model spectra have $E(B-V)$ of 0.0 or 0.4. Changes in completeness are found to be negligibly small in either case except for $Ri'z'$ LBGs. Next, we examined the effect of changing the absorption by the intergalactic medium. If we shift the amount of attenuation to $\pm 1\,\sigma$ from the average amount given by Madau (1995), we obtain quite different completeness values. However, the redshift distribution functions derived are unrealistic, because they are strongly inconsistent with the distributions of spectroscopic objects. We also adopted Meiksin's (2006) prescription for absorption by the intergalactic medium and found completeness values similar to those based on Madau's (1995).

3.4. Contamination by Interlopers

We estimate the fraction of low-redshift interlopers in the LBG samples by a Monte Carlo simulation as follows: For the boundary redshift, z_0, between interlopers and LBGs, $z_0 = 3.5$ is adopted for BRi' LBGs, $z_0 = 4.0$ for $Vi'z'$ LBGs, and $z_0 = 4.5$ for $Ri'z'$ LBGs.

We use objects in the Hubble Deep Field North (HDF-N), for which best-fit spectra and photometric redshifts are given by

TABLE 2
LBG Surveys in the Literature

Sample	Area (arcmin^2)	m_{limit}	N	Selection	Shown in This Paper	Reference
$z \sim 3$.............................	1046	$\mathcal{R} = 25.5$	1270	$U_n - G,\ G - \mathcal{R}$	Fig. 21	Steidel et al. 1999
$z \sim 4$.............................	828	$I = 25.0$	207	$G - \mathcal{R},\ \mathcal{R} - I$	Figs. 14, 19	Steidel et al. 1999
	543	$i' = 26.3$	1438	$B - R,\ R - i'$	Figs. 14, 19	Ouchi et al. 2004
	720	$I_C = 25.5$	?	$B - R,\ R - I_C$	Fig. 14	Capak et al. 2004
	169	$\mathcal{R} = 27.0$	427	$G - \mathcal{R},\ \mathcal{R} - I$	Fig. 19	Sawicki & Thompson 2006
	875	$i' = 26.85$	3808	$B - R,\ R - i'$	Figs. 14, 19, 21	This study
$z \sim 5$.............................	575	$I_C = 25.95$	305	$V - I_C,\ I_C - z'$	Figs. 15, 20	Iwata et al. 2003
	616	$z' = 25.8$	246	$V - i',\ i' - z'$	Figs. 15, 20	Ouchi et al. 2004
	720	$I_C = 25.5$	?	$V - I_C,\ I_C - z'$	Fig. 15	Capak et al. 2004
	616	$z' = 25.8$	68	$R - i',\ i' - z'$	Figs. 16, 20	Ouchi et al. 2004
	875	$z' = 26.05$	539	$V - i',\ i' - z'$	Figs. 15, 20, 21	This study
	875	$z' = 26.05$	240	$R - i',\ i' - z'$	Figs. 16, 20, 21	This study
$z \sim 6$.............................	12[a]	$z' = 29.5$	506	$i - z,\ V - z$	Fig. 21	Bouwens et al. 2006
	767	$z_R = 25.4$	12	$i' - z_R,\ z_B - z_R$	Fig. 21	Shimasaku et al. 2005

[a] Bouwens et al. (2006) incorporated the faint data from the Hubble Ultra Deep Field (12 arcmin^2) with two other data sets of shallower depth: the two GOODS fields (~ 170 arcmin^2 each) and the two Ultra Deep Field parallel fields (20 arcmin^2 in total).
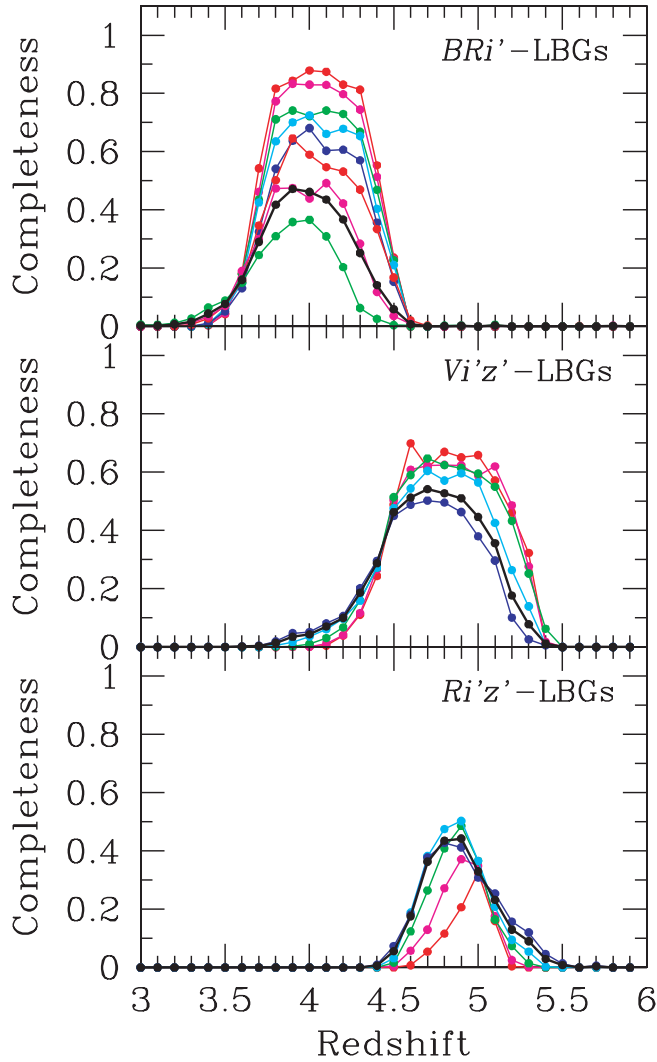
Fig. 17.—Completeness vs. redshift of objects with different apparent magnitudes for our LBG samples. In the BRi' LBG panel, the red, magenta, green, cyan, blue, red, magenta, and green (*top to bottom*) lines denote the completeness for $i' = 23.1, 23.6, 24.1, 24.6, 25.1, 25.6, 26.1,$ and 26.6, respectively. In the $Vi'z'$ and $Ri'z'$ LBG panels, the red, magenta, green, cyan, and blue lines denote the completeness for $z' = 23.8, 24.3, 24.8, 25.3,$ and 25.8, respectively. The thick black lines in all panels indicate the magnitude-weighted completeness.

Furusawa et al. (2000), as a template for the color, magnitude, and redshift distribution of foreground galaxies, and we generate 929 artificial objects that mimic the HDF-N objects. The apparent sizes of the artificial objects are adjusted so that the size distribution recovered from the simulation is similar to that of the real objects in our catalogs. We distribute the artificial objects randomly on the original images, after adding Poisson noise according to their magnitudes, and perform object detection and photometry in the same manner as employed for real objects. The sequence of these processes was repeated 100 times. In the simulation, the number of interlopers can be defined as the number of simulated objects with low redshift ($z < z_0$) that are detected and also satisfy the selection criteria for LBGs. The number of interlopers expected in an LBG sample can then be calculated by multiplying the raw number by a scaling factor that corresponds to the ratio of the area of the SDF (875 arcmin^2) to the area of the HDF-N multiplied by the number of repetitions (100×3.92 arcmin^2). Figure 18 shows the fraction of interlopers for our LBG samples as a function of magnitude. For the BRi' and $Ri'z'$ LBG samples,
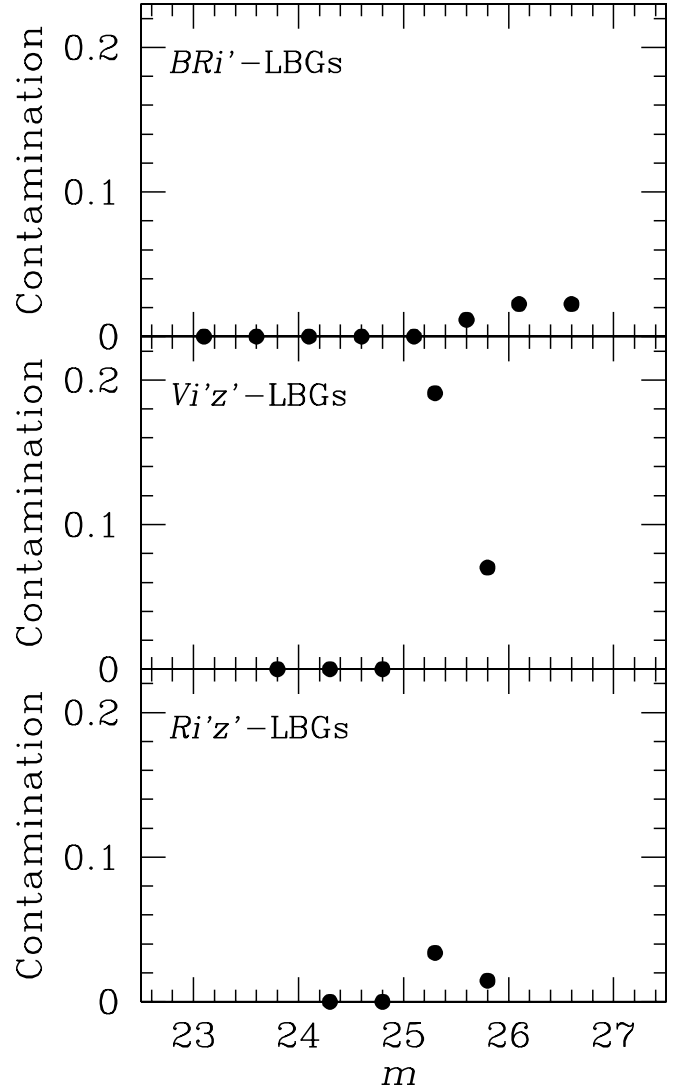

Fig. 18.—Fraction of interlopers as a function of magnitude for our LBG samples.

the fraction is found to be less than 5% at any magnitude. For the $Vi'z'$ LBG sample, the contamination is higher but at most $\simeq 20\%$. Most of the interlopers are in the redshift range $0.2 \leq z \leq 0.8$, as predicted from Figures 4–6. The rest are objects at redshifts that are close to the boundary redshift of each sample. The fraction of interlopers only at low redshift (i.e., not near the boundary redshifts) for each whole sample is around 1% for the BRi' and $Ri'z'$ LBG samples, and around 9% for the $Vi'z'$ LBG sample.

The number density and the redshift distribution of galaxies in the HDF-N may be largely different from the cosmic averages, because the HDF-N is a very small field. However, the contamination by interlopers for each of the three LBG samples calculated above is very low. We therefore expect that the uncertainty in contamination due to a possible (large) cosmic variance in the HDF-N galaxies will not be a significant source of the error in the luminosity functions of LBGs derived in the next section.

4. LUMINOSITY FUNCTIONS AT REST-FRAME ULTRAVIOLET WAVELENGTHS

We derive the luminosity functions of LBGs at $z \sim 4$–5 by applying the "effective volume" method (Steidel et al. 1999).

TABLE 3
NUMBER OF LBGs DETECTED, NUMBER OF INTERLOPERS,
AND EFFECTIVE SURVEY VOLUME FOR BRi' LBGs

Magnitude Range (i')	N_{raw}[a]	$N_{\mathrm{interloper}}$[b]	V_{eff}[c]
22.85–23.35	3	0	1.74×10^6
23.35–23.85	12	0	1.63×10^6
23.85–24.35	68	0	1.49×10^6
24.35–24.85	231	0	1.39×10^6
24.85–25.35	447	0	1.22×10^6
25.35–25.85	763	8.9	1.15×10^6
25.85–26.35	1093	24.6	8.77×10^5
26.35–26.85	1191	26.8	5.70×10^5

[a] Number of LBGs detected.
[b] Number of interlopers estimated from our simulations (see § 3.4).
[c] Effective survey volume for 875 arcmin² in units of Mpc³.

The Monte Carlo simulation in § 3.3 yields the effective survey volume as a function of apparent magnitude,

$$V_{\mathrm{eff}}(m) = \int_{z_0}^{\infty} p(m, z) \frac{dV(z)}{dz} \, dz, \qquad (4)$$

where $p(m, z)$ is the probability that a galaxy of apparent magnitude m at redshift z is detected and passes the selection criteria (i.e., the completeness in § 3.3 for magnitude m and redshift z), $dV(z)/dz$ is the differential comoving volume at redshift z for a solid angle of the surveyed area (875 arcmin²), and z_0 is the boundary redshift between low-redshift galaxies and LBGs. The effective volume obtained for each magnitude bin is provided in Tables 3–5.

The number density of LBGs corrected for incompleteness and contamination is computed as

$$\phi(m) = \frac{N_{\mathrm{raw}}(m) - N_{\mathrm{interloper}}(m)}{V_{\mathrm{eff}}(m)}, \qquad (5)$$

where $N_{\mathrm{raw}}(m)$ and $N_{\mathrm{interloper}}(m)$ are the number of LBGs detected and the number of interlopers estimated from the simulations, respectively, in an apparent magnitude bin of m. Tables 3–5 also give $N_{\mathrm{raw}}(m)$ and $N_{\mathrm{interloper}}(m)$.

The number densities of LBGs in faint bins, especially the faintest bins, could be largely overestimated owing to Eddington bias from objects in fainter bins or beyond the limiting magnitude of the sample, which have very large photometric errors and probably have a larger number density. We evaluate the effect of this bias for each LBG sample as follows: First, we construct a deeper sample of LBGs down to a magnitude limit fainter by 0.5 mag than the original value (e.g., the new limit is $i' \leq 27.35$

TABLE 4
NUMBER OF LBGs DETECTED, NUMBER OF INTERLOPERS,
AND EFFECTIVE SURVEY VOLUME FOR $Vi'z'$ LBGs

Magnitude Range (z')	N_{raw}[a]	$N_{\mathrm{interloper}}$[b]	V_{eff}[c]
23.55–24.05	1	0	1.34×10^6
24.05–24.55	12	0	1.31×10^6
24.55–25.05	56	0	1.31×10^6
25.05–25.55	152	29.0	1.17×10^6
25.55–26.05	318	22.3	9.66×10^5

[a] Number of LBGs detected.
[b] Number of interlopers estimated from our simulations (see § 3.4).
[c] Effective survey volume for 875 arcmin² in units of Mpc³.

TABLE 5
NUMBER OF LBGs DETECTED, NUMBER OF INTERLOPERS,
AND EFFECTIVE SURVEY VOLUME FOR $Ri'z'$ LBGs

Magnitude Range (z')	N_{raw}[a]	$N_{\mathrm{interloper}}$[b]	V_{eff}[c]
24.05–24.55	3	0	3.32×10^5
24.55–25.05	18	0	4.60×10^5
25.05–25.55	66	2.2	5.54×10^5
25.55–26.05	153	2.2	5.69×10^5

[a] Number of LBGs detected.
[b] Number of interlopers estimated from our simulations (see § 3.4).
[c] Effective survey volume for 875 arcmin² in units of Mpc³.

for BRi' LBGs). Then, using this deeper sample, we carry out Monte Carlo simulations similar to those made in § 3.3 and derive $V_{\mathrm{eff}}(m)$ in order to calculate $\phi(m)$ to a deeper magnitude. From the simulations, we compute for each magnitude bin the fractions of LBGs that scatter out to other magnitude bins. Finally, we recalculate $\phi(m)$ by correcting the original number densities for the scatter along the magnitude axis. The number density of LBGs derived in this way is found to be consistent with the original calculation within statistical errors, down to the original limiting magnitude. This means that Eddington bias is negligibly small for our samples.

The LF in the rest-frame ultraviolet ($\simeq 1500$ Å) absolute magnitude, M_{UV}, is obtained by converting $\phi(m)$ into $\phi(M_{\mathrm{UV}}(m))$. For each LBG sample, we calculate the absolute magnitude of LBGs from their apparent magnitude using the average redshift of the sample as

$$M_{\mathrm{UV}} = m + 2.5 \log(1 + \bar{z}) - 5 \log d_L(\bar{z}) + 5 + (m_{\mathrm{UV}} - m),$$

$$(6)$$

where d_L is the luminosity distance in units of parsecs. For the apparent magnitude m, we use i' magnitude for BRi' LBGs and z' magnitude for $Vi'z'$ and $Ri'z'$ LBGs. The last term in equation (6), $m_{\mathrm{UV}} - m$, is the difference between the magnitude at rest-frame 1500 Å and the magnitude in the bandpass being considered in the rest frame. Using the representative galaxy models given in § 3.1, we find $m_{\mathrm{UV}} - m$ to be negligible, or no larger than 0.03 mag, over the redshift ranges selected by the color selection criteria we adopt. Thus, we set $m_{\mathrm{UV}} - m$ to zero in equation (6). We assume that all the LBGs have the average redshift of the sample. Indeed, for each of the three LBG samples, varying the redshift of an object over the standard deviation of the redshift distribution of the sample changes its absolute magnitude by no more than 0.1 mag.

In Figures 19 and 20 the LFs at $z \sim 4$ and $z \sim 5$ are plotted, respectively, along with those from other authors (see Table 2). Note that Capak et al. (2004) do not derive the LFs. Our LFs are in excellent agreement with those of Ouchi et al. up to their faintest magnitudes for both redshifts. This agreement appears reasonable, since Ouchi et al. (2004) and this study are based on the same field (the SDF) and adopt almost the same selection criteria. Our LFs reach fainter magnitudes than theirs. However, there is a discrepancy between our $z \sim 4$ LF and that of Sawicki & Thompson (2006) in the Keck Deep Fields at the faint end; the faint-end slope of our LF is steeper than that of Sawicki & Thompson. Gabasch et al. (2004) also derived the galaxy LFs at rest-frame UV wavelengths in the FORS Deep Field, using photometric redshifts, and obtained a similar result to that of Sawicki & Thompson. The reason for this inconsistency is not clear. We note however that our raw counts before the correction for incompleteness already exceed Sawicki & Thompson's corrected
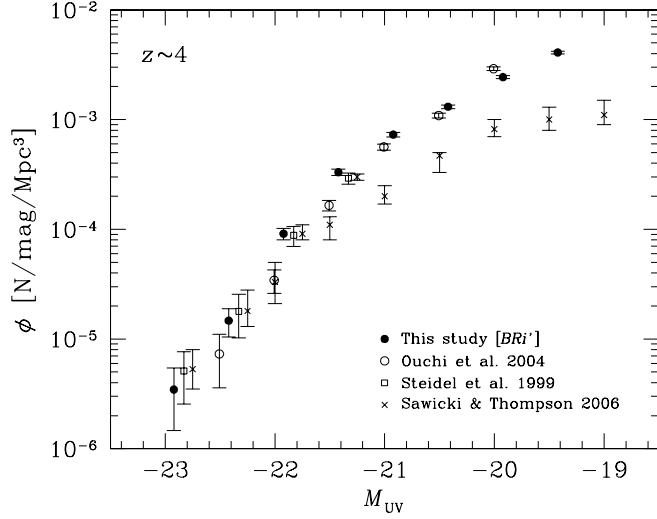
FIG. 19.—UV luminosity functions of LBGs at $z \sim 4$. Our data are shown by the filled circles. The open circles, squares, and crosses are from Ouchi et al. (2004), Steidel et al. (1999), and Sawicki & Thompson (2006), respectively. The error bars for our data and Ouchi et al.'s (2004) reflect Poisson errors, and those for the other two data include both Poisson errors and an estimate of field-to-field variance from their multiple fields.

counts, and thus our higher values are not due to overcorrections. In addition, our data have a sky coverage 5 times larger than that of the total of the five Keck Deep Fields. Thus, our LF is more robust against any possible cosmic variance on large scales, although the five separate Keck Deep Fields are less affected by cosmic variance than a single contiguous field of the same sky coverage. At $z \sim 5$, our LF is different from that of Iwata et al. (2003) at bright magnitudes. One possible explanation for this difference is that Iwata et al. may have selected a large number of contaminants, as mentioned in § 3.2, resulting in a higher number density of bright LBGs.

We find good agreement between our $z \sim 5$ LFs obtained from the $Vi'z'$ LBG sample and the $Ri'z'$ LBG sample. The redshift ranges of these two samples are almost the same. This consistency in the results from the two independent manners provides strong
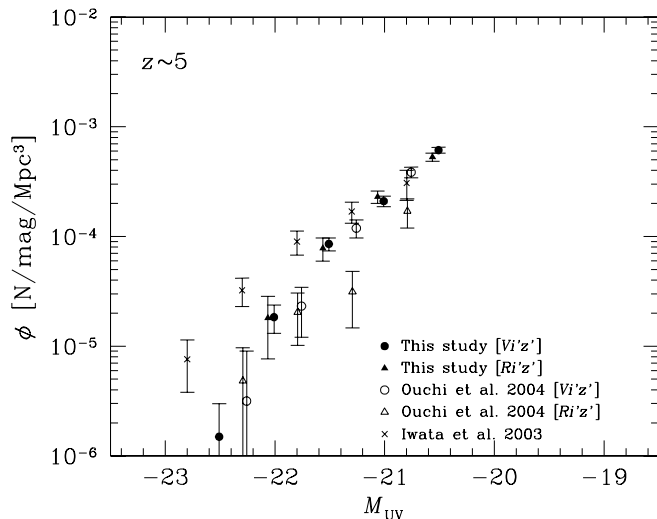

FIG. 20.—UV luminosity functions of LBGs at $z \sim 5$. Our data from the $Vi'z'$ and $Ri'z'$ LBG samples are shown by the filled circles and triangles, respectively. The open circles and triangles are from Ouchi et al.'s (2004) $Vi'z'$ LBG sample and $Ri'z'$ LBG sample, respectively. The crosses are from Iwata et al. (2003). The error bars reflect Poisson errors.

TABLE 6
LUMINOSITY FUNCTION PARAMETERS

Sample	$\bar{z}$	s_z	ϕ^* (10^{-3} Mpc^{-3})	M^*_{UV}	α
BRi' LBGs.........	4.0	0.3	$1.46^{+0.41}_{-0.35}$	$-21.14^{+0.14}_{-0.15}$	$-1.82^{+0.09}_{-0.09}$
$Vi'z'$ LBGs........	4.7	0.3	$0.58^{+1.04}_{-0.49}$	$-21.09^{+0.54}_{-0.74}$	$-2.31^{+0.68}_{-0.60}$
$Vi'z'$ LBGs........	4.7	0.3	$1.23^{+0.44}_{-0.27}$	$-20.72^{+0.16}_{-0.14}$	-1.82 (fixed)

support for the LFs we obtained. As the $Vi'z'$ LBG sample contains a statistically larger number of objects and has higher completeness, we only use results from this sample in the following analysis for $z \sim 5$. These LFs obtained at $z \sim 4$ and $z \sim 5$ are found to be well reproduced by a semianalytic model combined with high-resolution N-body simulations (Nagashima et al. 2005) when the observational selection effects are taken into account. We should, however, point out that the Lyman break technique cannot select all star-forming galaxies at a targeted redshift. On the basis of spectroscopy of galaxies in an optically selected, flux-limited sample, Le Fèvre et al. (2005) claim that a large fraction of galaxies at $z \sim 3-4$ lie outside the selection boundaries for LBGs in two-color diagrams. In addition, submillimeter-selected galaxies (e.g., Smail et al. 1997) and NIR-selected star-forming galaxies (e.g., Franx et al. 2003) are often too faint at optical wavelengths to be selected as LBGs, because of strong absorption by dust. Such dusty star-forming galaxies could contribute to the cosmic SFR density as much as do LBGs (see, e.g., Chapman et al. 2005). Therefore, the far-UV luminosity function and the SFR density derived in this paper are for galaxies with modest dust extinction and which pass the selection criteria for LBGs, and thus they might be greatly modified if all star-forming galaxies were included.

We fit the LFs with the Schechter (1976) function:

$$\phi(L)dL = \phi^* \left(\frac{L}{L^*}\right)^\alpha \exp\left(-\frac{L}{L^*}\right) d\left(\frac{L}{L^*}\right) \qquad (7)$$

or, expressed in terms of absolute magnitude,

$$\phi(M_{UV})dM_{UV} = \frac{\ln 10}{2.5} \phi^* (10^{-0.4(M_{UV}-M^*_{UV})})^{\alpha+1}$$
$$\times \exp\left(-10^{-0.4(M_{UV}-M^*_{UV})}\right) dM_{UV}, \qquad (8)$$

where ϕ^*, L^* (M^*_{UV}), and α are parameters to be determined from the data. The parameter ϕ^* is a normalization factor with dimensions of number density, L^* is a "characteristic luminosity" (with an equivalent "characteristic absolute magnitude," M^*_{UV}), and α gives the slope of the LF at the faint end. For the $z \sim 5$ LF, whose α has a rather large uncertainty, we evaluate ϕ^* and M^*_{UV} with α fixed to the best-fit value for the $z \sim 4$ LF, besides fitting with all three parameters left free. The best-fit parameters obtained are listed in Table 6.

5. EVOLUTION OF COSMIC STAR FORMATION ACTIVITY OVER $0 \leq z \leq 6$

5.1. Evolution of the Luminosity Function

We plot the LFs at $z \sim 4$ and $z \sim 5$ obtained in this study along with those of LBGs at $z \sim 3$ (Sawicki & Thompson 2006) and $z \sim 6$ (Bouwens et al. 2004; Shimasaku et al. 2005 [from observations of the SDF in new filters sensitive to $\simeq 1$ μm]) in Figure 21. The LFs of UV-selected (1500 Å) galaxies at $z \sim 0$ (Wyder et al. 2005) and $z \sim 1$ (Arnouts et al. 2005) are presented as well for reference. Figure 21 reveals clear evolution of the LF
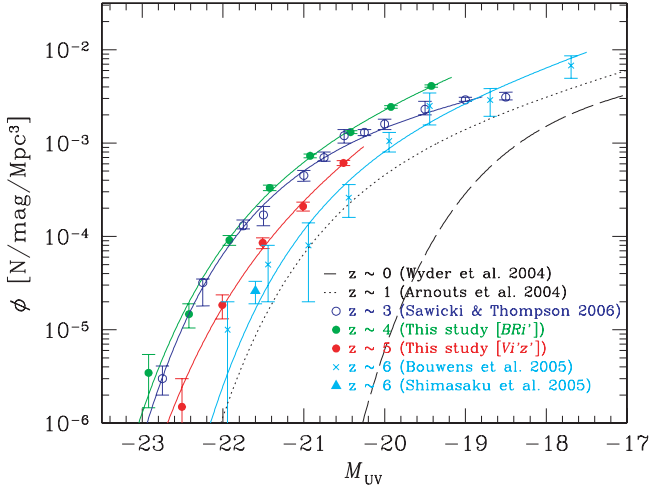
Fig. 21.—UV luminosity functions of LBGs at $z \sim 3$ (*blue circles*; Sawicki & Thompson 2006), $z \sim 4$ (*green circles*; this study [BRi' LBGs]), $z \sim 5$ (*red circles*; this study [$Vi'z'$ LBGs]), and $z \sim 6$ (*cyan crosses and triangle*; Bouwens et al. 2006; Shimasaku et al. 2005). The error bars reflect Poisson errors. The best-fit Schechter function is also shown (*solid lines*) for each data set, except for that of Shimasaku et al. (2005). The black dashed and dotted lines indicate the LFs of UV-selected galaxies at $z \sim 0$ (Wyder et al. 2005) and $z \sim 1$ (Arnouts et al. 2005), respectively.

beyond $z \sim 4$. From $z \sim 4$ to $z \sim 3$, we find no significant evolution over the whole luminosity range. Sawicki & Thompson (2006) and Gabasch et al. (2004) detected an increase in faint galaxies across this redshift interval, but such an increase is not seen in our data. At lower redshifts, luminous galaxies strongly decrease in number from $z \gtrsim 2$ to $z \sim 0$, as has been found in previous studies.

It is unlikely that the LF evolution seen in Figure 21 is caused by differences in selection criteria among the different samples. We find, using spectra of model galaxies, that the criteria for LBGs at redshifts of ~ 3, ~ 4, and ~ 5 select galaxies over similar ranges of age and $E(B-V)$. Since i'-dropout galaxies at $z \sim 6$ are selected with $i'-z'$ color alone, they can have a wide range of $E(B-V)$. However, since no observation has reported a significant increase in dust extinction at $z > 5$, it is reasonable to assume that the i'-dropout galaxies are a similar population to LBGs at lower redshifts. Galaxies at $z \lesssim 1$ are selected in completely different ways from the Lyman break technique. However, the differences in LF between $z \gtrsim 3$ and $z \lesssim 1$ seen in Figure 21 appear to be too large to be accounted for by possible selection effects. The dimming of the LF seen for $z \lesssim 1$ will at least be qualitatively correct.

Figure 22 shows the evolution of the Schechter parameters over $0 \leq z \leq 6$. The filled circles represent our measurements. The other symbols show measurements taken from the literature. Note that the measurements at $z \sim 2$ and $z \sim 3$ from Arnouts et al. (2005) may have large uncertainties, because they are based solely on the HDFs, which cover only a tiny area. The normalization factor ϕ^* and the faint-end slope α appear to be almost constant over the redshift range $0.5 \leq z \lesssim 6$, followed by a significant change at lower redshifts. We note that α at $z \sim 5$ is fixed to the value at $z \sim 4$ in evaluating the other two parameters, but the value at $z \sim 4$ is similar to that at $z \sim 6$. From $z \sim 0.5$ to $z \sim 0$, ϕ^* rises by half an order of magnitude and α becomes shallower, from -1.6 to -1.2. On the other hand, the characteristic magnitude M^* strongly and nonmonotonically evolves over $0 \leq z \leq 6$. It brightens by about 1 mag from $z \sim 6$ to $z \sim 4$ and remains unchanged to $z \sim 3$, and then a significant fading of about 3 mag
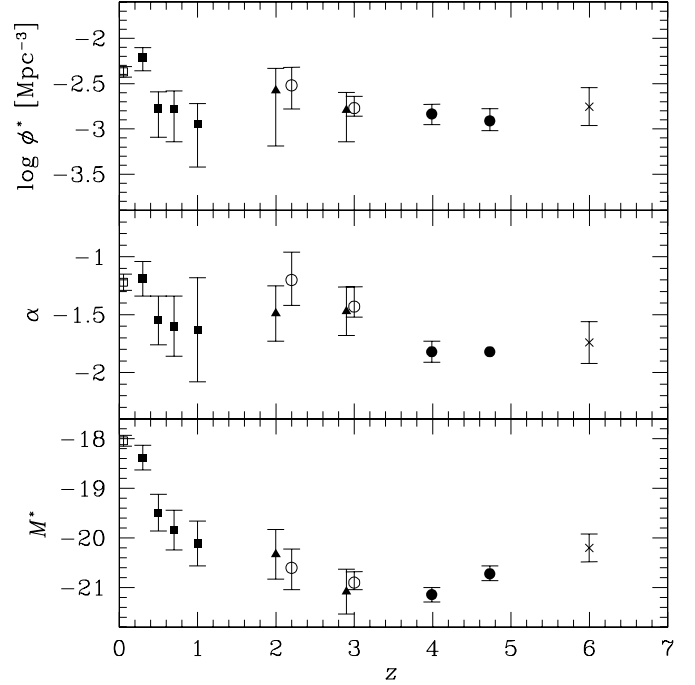

Fig. 22.—Evolution of the LF parameters with time. The filled circles represent the measurements from this study. The other symbols show measurements taken from the literature: *open squares*, Wyder et al. (2005); *filled squares*, Arnouts et al. (2005; *GALEX*); *triangles*, Arnouts et al. (2005; HDF); *circles*, Sawicki & Thompson (2006); *crosses*, Bouwens et al. (2006). For $z \sim 5$, we fixed α to the value at $z \sim 4$ ($\alpha = -1.82$) in evaluating the other two parameters.

occurs from $z \sim 3$ to $z \sim 0$. In other words, the evolution of the LF seen in Figure 21 is accounted for by a change in M^* with cosmic time. We point out, however, that there are different results about the LFs at $z \sim 4$ and $z \sim 5$, as mentioned in § 4. Some groups claim that the faint-end slope is shallower at higher redshifts (Iwata et al. 2003; Gabasch et al. 2004; Sawicki & Thompson 2006). The characteristic magnitude found by Sawicki & Thompson (2006) at $z \sim 4$ is consistent with ours. Iwata et al. (2003) obtained a value about 1 mag brighter at $z \sim 5$ than ours.

5.2. *Cosmic Star Formation Rate Density*

5.2.1. *Cosmic SFR Density beyond $z \sim 3$*

The UV luminosity density, ρ_L, at $z \sim 4$ and $z \sim 5$ is derived by integrating the LFs obtained in § 4 as

$$\rho_L = \int_{L_{\min}}^{\infty} L\phi(L)dL. \qquad (9)$$

We consider two kinds of luminosity density. One is the "observed" luminosity density, $\rho_L^{\rm obs}$, which is derived from integration down to the faintest luminosity of the sample, $L_{\min} = L_{\min}^{\rm obs}$. This quantity gives a lower limit on the true luminosity density. The faintest absolute magnitude of the sample at each redshift is $M_{\rm UV} = -19.2$ for $z \sim 4$ (BRi' LBGs) and $M_{\rm UV} = -20.3$ for $z \sim 5$ ($Vi'z'$ LBGs). The other is the luminosity density derived by integrating the LFs down to the same luminosity limit for all the measures. This is important to properly account for possible evolution. Following Steidel et al., we choose the limit to be $L_{\min} = 0.1 L_{z=3}^*$, where $L_{z=3}^*$ is the characteristic luminosity of the LF of $z \sim 3$ LBGs given by Steidel et al. (1999). The luminosity $0.1 L_{z=3}^*$ corresponds to $M_{\rm UV} = -18.6$. We refer to this quantity as $\rho_L^{L>0.1 L_{z=3}^*}$ hereafter. When calculating $\rho_L^{L>0.1 L_{z=3}^*}$, we extrapolate the Schechter functions derived in § 4 to

TABLE 7
Ultraviolet Luminosity Densities

Sample	$\bar{z}$	s_z	ρ_L (ergs^{-1} Hz^{-1} Mpc^{-3})	
			$\rho_L^{\rm obs}(M_{\rm UV} < M_{\rm limit})$[a]	$\rho_L^{L>0.1L^*_{z=3}}(M_{\rm UV} < -18.6)$
BRi' LBGs.......	4.0	0.3	$2.21^{+0.01}_{-0.01} \times 10^{26}$	$2.82^{+0.04}_{-0.04} \times 10^{26}$
$Vi'z'$ LBGs......	4.7	0.3	$4.33^{+0.03}_{-0.05} \times 10^{25}$	$1.85^{+0.99}_{-0.58} \times 10^{26}$

[a] Observed limiting magnitudes; $M_{\rm UV} = -19.2$ for BRi' LBGs and $M_{\rm UV} = -20.3$ for $Vi'z'$ LBGs.

fainter magnitudes than the observation limits. This extrapolation is modest for the $z \sim 4$ LBG sample (BRi' LBGs), since the $L_{\rm min}^{\rm obs}$ of this sample ($M_{\rm UV} = -19.2$) is close to $0.1L^*_{z=3}$, On the other hand, the extrapolation is large for the $z \sim 5$ LBG sample ($Vi'z'$ LBGs); $M_{\rm UV} = -18.6$ is fainter than the limiting magnitude of this sample by 1.7 mag. Table 7 presents $\rho_L^{\rm obs}$ and $\rho_L^{L>0.1L^*_{z=3}}$.

The UV luminosity density can be used to measure the star formation rate density in the universe. We compute the cosmic SFR density using the relationship between SFR and ultraviolet luminosity, $L_{\rm UV}$, given by Kennicutt (1998):

$$\mathrm{SFR}(M_\odot\ \mathrm{yr}^{-1}) = 1.4 \times 10^{-28} L_{\rm UV}(\mathrm{ergs\ s}^{-1}\ \mathrm{Hz}^{-1}). \quad (10)$$

This formula assumes a Salpeter initial mass function with $0.1\,M_\odot < M < 100\,M_\odot$. The SFR density is corrected for dust extinction following Hopkins (2004), who used the dust extinction formula of Calzetti et al. (2000) and assumed $E(B-V) = 0.128$ at all redshifts.

In Figure 23, we show the cosmic SFR densities obtained in this study as a function of redshift (*filled circles*) compared with those calculated from the LFs of LBGs at $3 \le z \le 6$ in the literature. We similarly integrate their LFs down to the observed limiting luminosities to obtain $\rho_L^{\rm obs}$ and down to $L = 0.1L^*_{z=3}$ to obtain $\rho_L^{L>0.1L^*_{z=3}}$, convert them to SFR densities using equation (10), and correct for the same amount of dust extinction to provide a fair comparison. The black symbols indicate $\rho_L^{L>0.1L^*_{z=3}}$, while the cyan symbols are for the lower limit, $\rho_L^{\rm obs}$. Note that the limiting
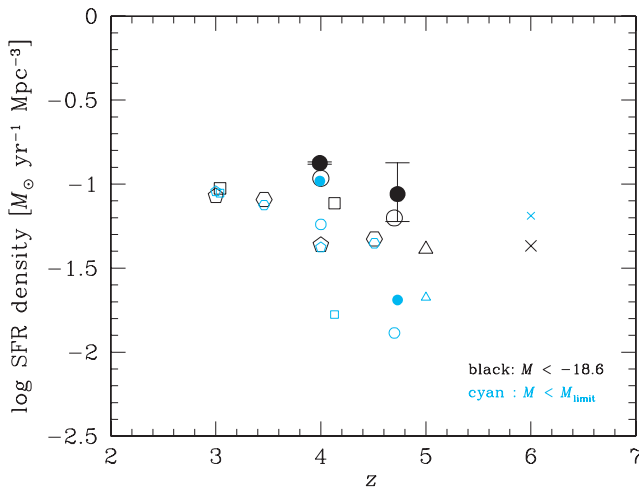

Fig. 23.—Cosmic SFR density as a function of redshift. The black symbols indicate the SFR densities calculated by integrating the luminosity functions down to $M_{\rm UV} = -18.6$ (equivalent to $L = 0.1L^*_{z=3}$ from Steidel et al. 1999), while the cyan symbols show the lower limits, i.e., the contribution from actually observed galaxies only. The filled circles represent the measurements from this study; the other points come from Steidel et al. (1999, *squares*), Iwata et al. (2003, *triangles*), Ouchi et al. (2004, *open circles*), Gabasch et al. (2004, *hexagons*), Sawicki & Thompson (2006, *pentagons*), and Bouwens et al. (2006, *crosses*).
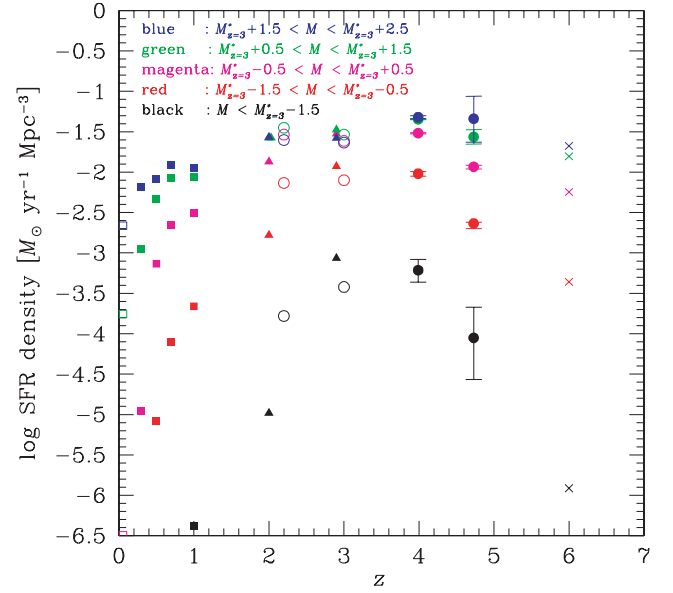

Fig. 24.—Cosmic SFR density as a function of redshift over the redshift range $0 \le z \le 6$, demonstrating the luminosity dependence of its evolution. The black, red, magenta, green, and blue symbols indicate the SFR density from galaxies with $M < M^*_{z=3}$, $M^*_{z=3} - 1.5 < M < M^*_{z=3} - 0.5$, $M^*_{z=3} - 0.5 < M < M^*_{z=3} + 0.5$, $M^*_{z=3} + 0.5 < M < M^*_{z=3} + 1.5$, and $M^*_{z=3} + 1.5 < M < M^*_{z=3} + 2.5$, respectively. The filled circles represent the measurements from this study. The open squares comes from Wyder et al. (2005), the filled squares from Arnouts et al. (2005; *GALEX*), the triangles from Arnouts et al. (2005; HDF), the open circles from Sawicki & Thompson (2006), and the crosses from Bouwens et al. (2006).

luminosity of the LF at $z \sim 6$ by Bouwens et al. (2006) is fainter than $0.1L^*_{z=3}$, resulting in $\rho_L^{\rm obs} > \rho_L^{L>0.1L^*_{z=3}}$. It can be seen that $\rho_L^{L>0.1L^*_{z=3}}$ is almost constant over $3 \lesssim z \lesssim 5$ and perhaps turns to decrease at a certain point between $z \sim 5$ and $z \sim 6$. It should be emphasized that the measurements of the SFR density at $z \sim 4$ and $z \sim 5$ are largely improved by this study. At $z \sim 4$, the observed SFR density is very close to $\rho_L^{L>0.1L^*_{z=3}}$, since our BRi' LBG sample reaches very close to $0.1L^*_{z=3}$. Thus, there is little uncertainty in our measurement of $\rho_L^{L>0.1L^*_{z=3}}$ at $z \sim 4$, while the previous measurements of the SFR density integrated to $0.1L^*_{z=3}$ have uncertainties of a factor of 2 or more due to a large extrapolation of the LF. From this figure, we can robustly conclude that the cosmic SFR density does not drop from $z \sim 3$ to $z \sim 4$, since the "observed" SFR density at $z \sim 4$ is not lower than $\rho_L^{L>0.1L^*_{z=3}}$ at $z \sim 3$. At $z \sim 5$, large errors owing to the uncertainty in the shape of the LFs at faint magnitudes still remain. However, from our observed SFR density, we can put a stronger constraint on the "decrease" in the cosmic SFR density from $z \sim 4$ to $z \sim 5$; the decrease, if any, cannot be larger than a factor of about 5.

5.2.2. Luminosity-dependent Evolution of the Cosmic SFR Density over $0 \le z \le 6$

We next examine the evolution of the cosmic SFR densities contributed from galaxies of different magnitudes over the redshift range $0 \le z \le 6$. Figure 24 compares their evolutionary behavior. The black, red, magenta, green, and blue symbols indicate the cosmic SFR densities from galaxies with magnitudes in the range $M < M^*_{z=3} - 1.5$, $M^*_{z=3} - 1.5 < M < M^*_{z=3} - 0.5$, $M^*_{z=3} - 0.5 < M < M^*_{z=3} + 0.5$, $M^*_{z=3} + 0.5 < M < M^*_{z=3} + 1.5$, and $M^*_{z=3} + 1.5 < M < M^*_{z=3} + 2.5$, respectively. The filled circles represent our measurements, and the other symbols show the values similarly calculated using LFs taken from the literature. There is a remarkable dependence of the evolutionary behavior of the SFR density on luminosity, as previously noted by Shimasaku

et al. (2005), who compared the evolution of the total cosmic SFR density and the SFR density from galaxies brighter than $M = -21.3$ to find that the SFR density from bright galaxies drastically changes with time. From Figure 24, it can be seen that the SFR density from fainter galaxies evolves more mildly. In addition, the peak position varies with luminosity; the contribution from fainter galaxies peaks at earlier epochs. For example, the SFR density for galaxies with $M^*_{z=3} - 1.5 < M < M^*_{z=3} - 0.5$ rises by about an order of magnitude from $z \sim 6$ to $z \sim 4$, remains unchanged to $z \sim 3$, and then drops by more than 3 orders of magnitude to the present epoch, thus having a sharp peak at $z \sim 3-4$. On the other hand, the SFR density for galaxies with $M^*_{z=3} + 1.5 < M < M^*_{z=3} + 2.5$ is almost constant within a factor of about 2 at $z \gtrsim 2$ with a blunt peak at $z \sim 4-5$. Iwata et al. (2003), Gabasch et al. (2004), and Sawicki & Thompson (2006) have reported different evolutions of the LBG luminosity function from $z \sim 4$ or 5 down to 3 from what we find in the SDF. At $3 \lesssim z \lesssim 5$, the luminosity density from these authors shows an opposite trend of fainter galaxies evolving more rapidly. However, it is at $z \lesssim 3$ and $z \gtrsim 5$ that the most drastic evolution occurs in the luminosity density. Thus, using the LFs from these authors does not qualitatively change the results on the overall $0 \lesssim z \lesssim 6$ evolution obtained here.

This luminosity-dependent evolution of the cosmic SFR density reflects the evolution of the LF, as discussed in § 5.1. The strong increase in SFR density for galaxies brighter than $M^*_{z=3} - 0.5$ from $z \sim 6$ to $z \sim 3$ is due to the brightening of M^* with time. The SFR densities for these bright galaxies then drop to the present epoch, as M^* fades during the same period. The evolution of the SFR densities for galaxies fainter than $M^*_{z=3} - 0.5$ is mild, since they are less sensitive to the change in M^*. The earlier peak position of the SFR density of fainter galaxies suggests that faint galaxies are more dominant in terms of the cosmic SFR density at earlier epochs.

We cannot completely rule out the possibility that the luminosity-dependent evolution in the cosmic SFR density seen above is not real but instead reflects the luminosity-dependent evolution of some other property such as dust extinction. If, for instance, galaxies have the smallest dust extinction at $z \sim 3-4$, then the observed M^* will be the brightest at these redshifts, as seen in Figure 22, even if the intrinsic, dust-corrected M^* does not change with redshift. In this case, the behavior of the luminosity-dependent SFR density will be qualitatively similar to that found in Figure 24. However, no observation has reported strong evolution of $E(B-V)$, at least for LBGs. The $E(B-V)$ distribution of LBGs appears to be unchanged from $z \sim 5$ to $z \sim 3$ (Iwata et al. 2003; Ouchi et al. 2004). In addition, $E(B-V)$ is known to be independent of apparent magnitude (Adelberger & Steidel 2000; Ouchi et al. 2004).

5.3. Specific Star Formation Rate

We now explore the evolution of what we define as the specific SFR here, that is, the cosmic SFR per unit baryon mass in dark halos. The specific SFR means the efficiency of star formation averaged over all the dark halos present at a given redshift. The specific SFR is computed by dividing the cosmic SFR density, $\rho_L^{L>0.1L^*_{z=3}}$, by the average mass density of baryons confined in dark halos, ρ_b. Here ρ_b is calculated by

$$\rho_b(z) = \frac{\Omega_b}{\Omega_m} \int_{M_{\min}(z)}^{\infty} n(M, z) M \, dM, \quad (11)$$

where $\Omega_b = 0.05$ is the density parameter of baryons, $n(M, z)$ is the mass function of dark halos at redshift z predicted by the
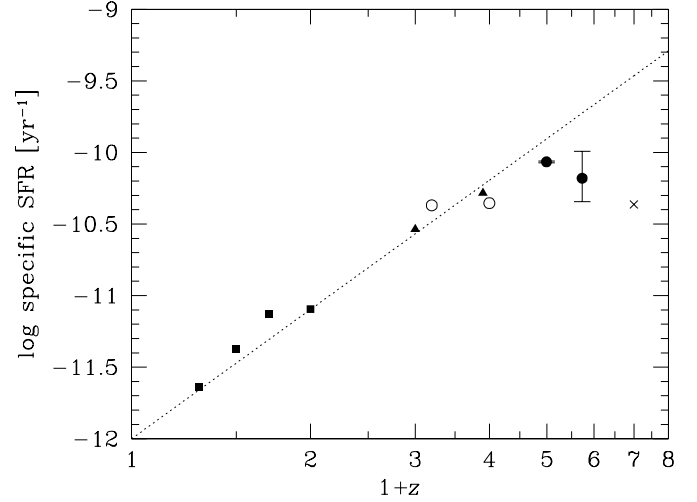

FIG. 25.—Specific SFR vs. $1 + z$ over $0 \leq z \leq 6$. Symbols are the same as in Fig. 24. The dotted line shows evolution in power-law, specific SFR $\propto (1 + z)^3$.

standard cold dark matter model with $\sigma_8 = 0.9$, and $M_{\min}(z)$ is the halo mass corresponding to a virial temperature of 1×10^4 K. We assume here that gas does not cool (and thus stars are not formed) in dark halos with $T < 1 \times 10^4$ K. Note that $M_{\min}(z)$ is much smaller than the estimated mass of halos that host the faintest galaxies we take into account here, that is, galaxies with $0.1L^*_{z=3}$.

Figure 25 shows the evolution of the specific SFR over $0 \leq z \leq 6$. The filled circles represent our measurements, and the other symbols show the values from the literature. The dotted line in the figure shows $(1 + z)^3$ evolution. We find that the specific SFR increases in proportion to $(1 + z)^3$ up to $z \sim 4$. In other words, the star formation efficiency in the universe rises with redshift. At $z \gtrsim 4$, on the other hand, the specific SFR appears to decrease.

Here, according to the standard cold dark matter model, the average internal density in physical units of baryons in dark halos virialized at a given redshift, $\langle \rho_b^{DH} \rangle$, is known to be approximately proportional to the average mass density of the universe at that time, and the average mass density of the universe changes as $(1 + z)^3$. Therefore, this implies that the specific SFR increases approximately in proportion to $\langle \rho_b^{DH} \rangle$ up to $z \sim 4$. Put another way, since the specific SFR is the internal density of SFR in dark halos, $\langle \rho_{SFR}^{DH} \rangle$, divided by $\langle \rho_b^{DH} \rangle$, this result can be expressed in terms of $\langle \rho_{SFR}^{DH} \rangle$ and $\langle \rho_b^{DH} \rangle$ as

$$\langle \rho_{SFR}^{DH} \rangle \propto \langle \rho_b^{DH} \rangle^2. \quad (12)$$

It is surprising that the star formation in galaxies obeys such a simple power law over 90% of cosmic history ($0 < z \lesssim 4$). Equation (12) resembles the Schmidt (1959) law for nearby disk galaxies, a relationship between the disk-averaged SFR and cold gas surface densities of $\Sigma_{SFR} = \text{const} \times \Sigma_{gas}^N$ with $N \sim 1.4$ (Kennicutt 1998).

We present here one possible explanation of the observed behavior of the specific SFR. The analytical modeling of galaxy formation by Hernquist & Springel (2003) based on the cold dark matter model shows that the gas cooling rate, $\dot{M}_{cool}/M_{DH}$, of dark halos roughly scales with $H(z)^2$ or, equivalently, with $(1 + z)^3$, as $H(z)$ is approximately proportional to $(1 + z)^{3/2}$ in our cosmology. They also find that the star formation rate in dark halos scales with the cooling rate at low and intermediate redshifts, while it changes to no longer be dependent on the cooling rate at redshifts larger than a certain limit, where the internal density of halos is so high

that the cooling time is shorter than the rate of consumption of cooled gas into stars. If we adopt this modeling, then our result implies that the cosmic SFR is primarily determined by the gas cooling rate at $z \lesssim 4$, while it is governed by the conversion rate of cooled gas into stars at larger redshifts.

Of course, the cooling rate may not be the major factor determining the cosmic star formation rate. There are many other factors on which star formation in galaxies can greatly depend, such as feedback by galactic winds, the UV background radiation field, and environmental effects such as galaxy merging and interactions. Since the relative importance of these factors will vary with the mass of dark halos, it will be interesting to measure the specific SFR as a function of halo mass.

6. SUMMARY AND CONCLUSIONS

We have investigated the luminosity functions and star formation rates of Lyman break galaxies at $z \sim 4$ and $z \sim 5$ based on the optical imaging data obtained in the Subaru Deep Field project. The SDF project is a program conducted by Subaru Observatory to carry out a deep and wide survey of distant galaxies.

Three samples of LBGs in a contiguous 875 arcmin^2 area were constructed. One consists of LBGs at $z \sim 4$ selected with the $B-R$ versus $R-i'$ diagram (BRi' LBGs). The other two consist of LBGs at $z \sim 5$ selected with two kinds of two-color diagram: $V-i'$ versus $i'-z'$ ($Vi'z'$ LBGs) and $R-i'$ versus $i'-z'$ ($Ri'z'$ LBGs). The number of LBGs detected is 3808 for BRi' LBGs, 539 for $Vi'z'$ LBGs, and 240 for $Ri'z'$ LBGs. The adopted selection criteria are proved to be fairly reliable by the spectroscopic data. We use Monte Carlo simulations to estimate the completeness and the fraction of contamination by interlopers. The redshift distribution functions obtained from the simulations exhibit good consistency with the redshift distributions of spectroscopically identified objects in the LBG samples.

We derived the luminosity functions at rest-frame ultraviolet wavelengths down to as faint as $M_{\rm UV} = -19.2$ at $z \sim 4$ and $M_{\rm UV} = -20.3$ at $z \sim 5$. The cosmic star formation rate density was measured from the UV luminosity density derived by integrating the luminosity functions. On the basis of the observed SFR density and the standard cold dark matter model, the cosmic SFR per unit baryon mass in dark halos—that is, the specific SFR—was computed. Combining the results obtained in this work with those taken from the literature, we reach the following conclusions:

1. Clear evolution of the luminosity function is detected. The characteristic magnitude M^* changes strongly over the redshift range $0 \leq z \leq 6$. It brightens by about 1 mag from $z \sim 6$ to $z \sim 4$, remains unchanged to $z \sim 3$, and then fades by about 3 mag from $z \sim 3$ to $z \sim 0$. On the other hand, the normalization factor, ϕ^*, and the faint-end slope, α, are almost constant over $0.5 \lesssim z \lesssim 6$.

2. The measurements of the SFR density at $z \sim 4$ and $z \sim 5$ have been greatly improved, since the luminosity functions are derived down to very faint magnitudes. Hence, the evolutionary behavior of the SFR density is more constrained. The cosmic SFR density does not drop from $z \sim 3$ to $z \sim 4$, and the decrease from $z \sim 4$ to $z \sim 5$, if any, cannot be larger than about a factor of 5.

3. The SFR density contributed from brighter galaxies changes more drastically with cosmic time. The contribution from galaxies brighter than $M^*_{z=3} - 0.5$ has a sharp peak around $z = 3$–4, while that from galaxies fainter than $M^*_{z=3} - 0.5$ evolves relatively mildly with a broad peak at earlier epochs. This luminosity-dependent evolution of the cosmic SFR density suggests that the galaxy population contributing to the total SFR density in the universe varies with time, reflecting the evolution of the luminosity function.

4. The specific SFR is found to scale with redshift as $(1 + z)^3$ up to $z \sim 4$, implying that the efficiency of star formation is on average higher at higher redshift, in proportion to the cooling rate within dark halos. It seems that this is not simply the case at $z \gtrsim 4$.

REFERENCES

Adelberger, K. L., & Steidel, C. C. 2000, ApJ, 544, 218
Arnouts, S., et al. 2005, ApJ, 619, L43
Bertin, E., & Arnouts, S. 1996, A&AS, 117, 393
Bouwens, R. J., Illingworth, G. D., Blakeslee, J. P., & Franx, M. 2006, ApJ, 653, 53
Bouwens, R. J., et al. 2004, ApJ, 606, L25
Bunker, A. J., Stanway, E. R., Ellis, R. S., & McMahon, R. G. 2004, MNRAS, 355, 374
Calzetti, D., Armus, L., Bohlin, R. C., Kinney, A. L., Koornneef, J., & Storchi-Bergmann, T. 2000, ApJ, 533, 682
Capak, P., et al. 2004, AJ, 127, 180
Chapman, S. C., Blain, A. W., Smail, I., & Ivison, R. J. 2005, ApJ, 622, 772
Dickinson, M., et al. 2004, ApJ, 600, L99
Faber, S. M., et al. 2003, Proc. SPIE, 4841, 1657
Franx, M., et al. 2003, ApJ, 587, L79
Furusawa, H., Shimasaku, K., Doi, M., & Okamura, S. 2000, ApJ, 534, 624
Gabasch, A., et al. 2004, A&A, 421, 41
Guhathakurta, P., Tyson, J. A., & Majewski, S. R. 1990, ApJ, 357, L9
Gunn, J. E., & Stryker, L. L. 1983, ApJS, 52, 121
Hernquist, L., & Springel, V. 2003, MNRAS, 341, 1253
Hopkins, A. M. 2004, ApJ, 615, 209
Iwata, I., Ohta, K., Tamura, N., Ando, M., Wada, S., Watanabe, C., Akiyama, M., & Aoki, K. 2003, PASJ, 55, 415
Iye, M., et al. 2004, PASJ, 56, 381
Kashikawa, N., et al. 2002, PASJ, 54, 819
———. 2003, AJ, 125, 53
———. 2004, PASJ, 56, 1011
———. 2006, ApJ, 637, 631
Kennicutt, R. C., Jr. 1998, ARA&A, 36, 189
Kodama, T., & Arimoto, N. 1997, A&A, 320, 41

Le Fèvre, O., et al. 2005, Nature, 437, 519
Lehnert, M. D., & Bremer, M. 2003, ApJ, 593, 630
Madau, P. 1995, ApJ, 441, 18
Maihara, T., et al. 2001, PASJ, 53, 25
Meiksin, A. 2006, MNRAS, 365, 807
Nagashima, M., Yahagi, H., Enoki, M., Yoshii, Y., & Gouda, N. 2005, ApJ, 634, 26
Miyazaki, S., et al. 2002, PASJ, 54, 833
Oke, J. B., & Gunn, J. E. 1983, ApJ, 266, 713
Ouchi, M. 2003, Ph.D. thesis, Univ. Tokyo
Ouchi, M., et al. 2004, ApJ, 611, 660
Papovich, C., Dickinson, M., & Ferguson, H. C. 2001, ApJ, 559, 620
Sawicki, M., & Thompson, D. 2006, ApJ, 642, 653
Schechter, P. 1976, ApJ, 203, 297
Schlegel, D. J., Finkbeiner, D. P., & Davis, M. 1998, ApJ, 500, 525
Schmidt, M. 1959, ApJ, 129, 243
Shimasaku, K., Ouchi, M., Furusawa, H., Yoshida, M., Kashikawa, N., & Okamura, S. 2005, PASJ, 57, 447
Smail, I., Ivison, R. J., & Blain, A. W. 1997, ApJ, 490, L5
Spergel, D. N., et al. 2003, ApJS, 148, 175
Stanway, E. R., Bunker, A. J., & McMahon, R. G. 2003, MNRAS, 342, 439
Steidel, C. C., Adelberger, K. L., Giavalisco, M., Dickinson, M., & Pettini, M. 1999, ApJ, 519, 1
Steidel, C. C., Adelberger, K. L., Shapley, A. E., Pettini, M., Dickinson, M., & Giavalisco, M. 2003, ApJ, 592, 728
Steidel, C. C., & Hamilton, D. 1992, AJ, 104, 941
Wyder, T. K., et al. 2005, ApJ, 619, L15
Yagi, M., Kashikawa, N., Sekiguchi, M., Doi, M., Yasuda, N., Shimasaku, K., & Okamura, S. 2002, AJ, 123, 66
Yan, H., Windhorst, R. A., & Cohen, S. H. 2003, ApJ, 585, L93